Computational Imaging for Dynamic Metasurface based Synthetic Aperture Radars

Sandamali Devadithya

A thesis submitted in partial fulfillment of the
requirements for the degree of

Master of Science in Electrical Engineering

University of Washington

2017

Committee:

Matthew S. Reynolds, Chair

Arka Majumdar

Program Authorized to Offer Degree:
Electrical Engineering

University of Washington

Abstract

Computational Imaging for Dynamic Metasurface based Synthetic Aperture Radars

Sandamali Devadithya

Chair of the Supervisory Committee:
Associate Professor Matthew S. Reynolds
Department of Electrical Engineering
Paul G. Allen School of Computer Science and Engineering

In this thesis, computational imaging is used to improve millimeter-wave dynamic metasurface based synthetic aperture radar (SAR) imaging.

SAR image reconstruction is a computationally complex inverse problem, which can be solved via a generalized inverse [e.g. full pseudoinverse (FPI)], or by means of approximation [e.g. matched filter (MF)]. However, approximation limits the resolution. In the first part of the thesis, a computationally efficient partitioned inverse (PI) algorithm for SAR image reconstruction is proposed. The independent partitions can be reconstructed in parallel using the matched filter or the pseudo inverse. A parallelized approach leveraging a graphics processing unit (GPU) is used to achieve a dramatic speedup compared to non-GPU accelerated algorithms. In the results presented in this thesis, PI algorithms are three orders magnitude faster than the FPI and two orders faster than the MF. The improved resolution of FPI is maintained by using the pseudo inverse to find the solutions for the PI. The partitioned pseudo inverse (PPI) algorithm is based on the Moore-Penrose pseudo inverse using truncated singular value decomposition for regularization. Optimal regularization ensures that the algorithm is robust to noise. It is shown that the PPI has an improved resolution of 24% over MF even at a signal to noise ratio (SNR) of 0 dB. Experimental results using a laboratory K-band (15-26.5 GHz) ultra-wideband SAR system are presented to validate the PI algorithms.

The second part of the thesis focuses on SAR imaging with dynamic metasurface antennas (DMAs). An enhanced resolution stripmap mode (ERSM) SAR approach is extended for 3D imaging using DMA, where PI algorithms are used to accelarate the reconstruction. Experimental results using a commercial prototype DMA are presented. It is shown that the cross-range resolution and ground-range resolution has improved by 26% and 42% respectively when using 3D ERSM SAR. Furthermore, the PI reconstruction resulted in a 23.5X speedup over the MF. A limitation of using DMAs for SAR imaging are strong side lobes of the antenna, which causes the images to be smeared due to a distorted point spread function (PSF). It is shown that Lucy-Richardson deconvolution using a measured PSF can be applied to correct the smearing, achieve high resolution, and restore the image. Experimental results using a liquid-crystal based DMA for near field SAR imaging are presented, where the reconstructed images are restored using Lucy-Richardson deconvolution.

TABLE OF CONTENTS

LIST OF FIGURES

LIST OF ABBREVIATIONS

AESA: Active electronically scanned array

ERSM: Enhanced resolution stripmap mode

FPI: Full pseudo-inverse

GPU: Graphic processing unit

MF: Matched filter

DMA: Dynamic metasurface antenna

PESA: Passive electronically scanned array

PI: Partitioned inverse

PMF: Partitioned matched filter

PPI: Partitioned pseudo-inverse

PSF: Point spread function

SAR: Synthetic aperture radar

SNR: Signal to noise ratio

SVD: Singular value decomposition

TSVD: Truncated singular value decomposition

ACKNOWLEDGMENTS

First and foremost, I would like to thank my graduate advisor Matt Reynolds, who had faith in me and was a constant source of support and encouragement during the past year. Always friendly and approachable, Matt's help was extremely useful not only in the research path which led to this thesis, but on adjusting to life as a grad student.

A special thanks go Andreas Pedross-Engel, my research supervisor, mentor, guide, and friend. Andreas's passion and dedication inspired me to find my own passion for research and I am forever grateful for him for his endless patience and guidance.

None of this research would have been possible without the collaboration of Claire. Her willingness to help at all times is remarkable. A shout out goes to everyone in Reynolds lab for the fun and laughter and the intellectual feedback. It was indeed a truly amazing journey with all of you.

Thank you for my thesis committee Arka Majumdar, for his valuable insights.

I am forever indebted to my parents and my family for all the sacrifices they have made and will make, to help me in everything I do. I was lucky to be born into a such a beautiful family. I also want to thank my fiance Maleen, for standing strong with me at all times.

A special thanks go to my brother Tharaka, and his wife Deepthi, for welcoming me to their home and making it my home away from home. Going there during the weekends was the best. My adorable nephews Lavindu and Hiruna ensured that I always have something to look forward to when the going got tough.

DEDICATION

to my incomparable parents

Chapter 1

INTRODUCTION

1.1 Overview

Synthetic aperture radar (SAR) images are representations of the microwave or millimeter-wave reflectivity of the observed scenes. Radar images can be obtained at any time during day and night, and through impairments such as fog, clouds, and sand-storms. Hence, it is complimentary to optical imaging. Microwave and millimeter wave imaging was originally developed for reconnaissance and military use. Now it has evolved into more general applications involving remote sensing, surveillance, and security [1, 2, 3].

SAR image reconstruction is an inverse problem. The reflection coefficients of the point scatterers of the scene needs to be estimated from the observed measurements. SAR uses a moving antenna platform to collect measurements from a scene. This accumulates a large number of data and the processing is computationally costly in both memory and time. The inverse can be estimated via an approximation, e.g. matched filter (MF), or a generalized inverse, e.g. pseudo inverse. The computation of the pseudo inverse is itself computationally complex. Therefore, with the constraints of standard PCs, image reconstruction using the pseudo inverse is not feasible in many cases. Even with the matched filter, for 3D images with millions of voxels, the reconstruction takes a considerable time on standard PCs. Furthermore since the matched filter is an approximation, the achievable resolution is limited [4].

In this thesis a partitioned inverse (PI) algorithm is proposed, which avoids the time and memory constrains of the generalized inverse. The approach divides the system model based on geometry, finds the inverse solution for each part separately, and coherently sums the solutions to reconstruct the final image. The matched filter or the pseudo inverse is used to find the inversion of the partitions. Solving for each partition can be done in parallel as they are independent, and hence, enables an efficient usage of a graphic processing unit (GPU). The algorithm is two orders faster than the widely used matched filter. Furthermore it is three orders faster than full pseudo inverse, which is not a feasible solution in most standard PCs. The improved resolution of a generalized inverse can be maintained if the pseudo inverse is used to find the solutions for the partitioned inverse. The partitioned pseudo inverse algorithm is based on the Moore-Penrose pseudo inverse using truncated singular value decomposition for regularization. Optimal regularization ensures that the algorithm is robust to noise. It is shown that the partitioned pseudo inverse has an improved resolution of 24% over matched filter even at 0 dB SNR. This work is published in [5, 6].

For spotlight mode SAR and other novel imaging SAR modes proposed in literature [7, 8, 9] beam steering of the radar antennas is required. Dynamic metasurface antennas (DMA) provide many advantages over the traditional electronic beam steering antennas, such as generating more diverse beam patterns with less hardware complexity. Therefore, DMAs have shown to be a promising approach for SAR imaging [3, 9, 10, 11]. In this thesis, computational imaging is used to improve millimeter wave SAR imaging for DMAs.

In [8] an enhanced resolution stripmap mode (ERSM) for DMAs was introduced to achieve a finer cross-range resolution while maintaining a larger coverage scene (as with standard stripmap mode SAR), and proof of concept experimental results were presented for 2D SAR imaging. In this work ERSM is extended to 3D SAR imaging. The idea of ERSM SAR is to create a large virtual antenna beamwidth by steering the antenna. However this increases the number of measurements collected and the reconstruction is even more computationally complex than the standard stripmap mode SAR. Therefore PI algorithms are applied to accelerate the image reconstruction. Laboratory experiments using DMAs show that the cross-range resolution is improved by 26% with 3D ERSM SAR. Furthermore, the ground-range information is also improved by 42%. Using the conventional matched filter approach, it is shown that the 3D ERSM reconstruction with GPU acceleration took 41.9 hours while the PI reconstruction took 1.78 hours and 1.93 hours for matched filter and pseudo inverse, respectively, resulting in a 23.5X speedup.

A limitation with the use of DMAs are strong antenna side lobes. In [10] results of using a liquid-crystal based DMA for near field SAR imaging was presented. However, due to the effect of side lobes in the radiation pattern the obtained SAR images are smeared by the distorted point spread function (PSF). This work shows that Lucy-Richardson deconvolution using a measured PSF can be applied to correct the smearing, achieve high resolution and restore the image. Furthermore the reconstruction is accelerated for the strip map mode imaging with the use of PI algorithms.

1.2 Outline of the Thesis

The outline of this thesis is as follows.

Chapters 2 and 3 give the theoretical background on SAR imaging and the inverse problem. In Chapter 4, the PI algorithm is introduced, its mathematical model is developed and analyzed using resolution matrices and point spread functions. In Chapter 5 experimental results using a laboratory K-Band (15-26.5 GHz) ultra-wideband SAR system are presented to validate the algorithm with 2D and 3D imaging results. As the proposed method allows for parallel processing, a GPU is utilized to achieve a dramatic speedup.

Chapters 6 and 7 are on SAR imaging with DMA. In Chapter 6 3D ERSM SAR is carried out on a commercial prototype DMA and PI algorithms are applied to accelerate the image reconstruction. Experimental results are presented to validate the concept. In Chapter 7 results of using a liquid-crystal based commercial prototype DMA for SAR imaging are presented. Lucy-Richardson deconvolution is applied to correct the image smearing introduced by distorted PSF, and achieve high resolution. Once again the reconstruction is accelerated for strip-map mode imaging using PI algorithms.

Finally in Chapter 8, the proposed algorithm and results are summarized and promising directions for future work is discussed.

Chapter 2

SYNTHETIC APERTURE RADAR

This chapter introduces synthetic aperture radar (SAR) imaging. The geometry of a SAR imaging system is described along with the resolution limits of the widely used reconstruction algorithms. The image reconstruction methods proposed in literature and used in practice are classified and summarized under the categories of inverse filtering and approximation methods. Furthermore, a brief description of dynamic metasurface antennas and its advantage for SAR imagery are discussed.

Some content of this chapter has appeared in previous work of the author [5, 6].

2.1 SAR Overview

Synthetic aperture radar (SAR) imaging was originally developed for reconnaissance and military use [12]. The oldest form of SAR is stripmap mode SAR (see Fig. 2.1), where an airborne or space-borne radar platform moves along a trajectory while gathering measurements from a strip on the ground. Another often used form of SAR is spotlight mode SAR, where the antenna is always steered to illuminate a single spot in the ground. The received signals are then typically processed using 2D correlation algorithms [13, 14] to obtain the SAR images. The resolution in the images of the spotlight mode SAR is better than of the stripmap mode SAR, but the coverage of the scene is limited with spotlight mode SAR [14].

SAR images are representations of the microwave or millimeter-wave reflectivity of the observed scenes. Due to the penetrating abilities of radio frequency signals in the microwave and millimeter-wave bands, SAR applications have evolved to more general radar imaging applications involving earth monitoring, remote sensing, surveillance, and security [1, 2, 3]. These applications are not limited to 2D and many involve 3D imaging.

2.2 Basics of SAR

2.2.1 SAR Geometry

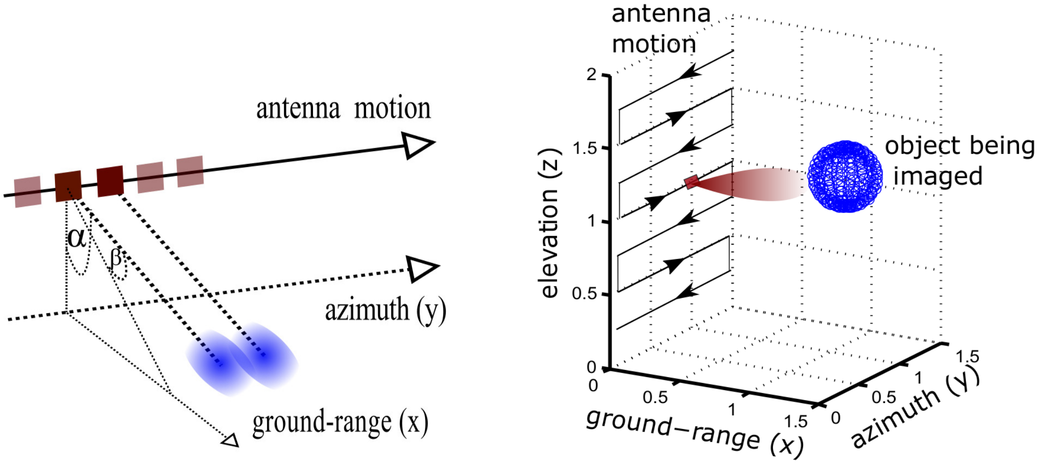

(a) (b)

Figure 2.1: Illustration of a strip-map mode SAR imaging system: (a) 1D scan to image a 2D scene (α is the looking angle, β is the squint angle), (b) 2D scan to image a 3D scene (looking angle α is 90°).

SAR uses a moving antenna platform to gain information from a scene. Fig. 2.1 depicts the geometric models for a mono-static SAR configuration, imaging 2D and 3D scenes. The radar antenna transmits a signal to illuminate the scene within its antenna beamwidth. The scene is comprised of hypothesized point-scatterers which backscatter some of the transmitted energy, which is then received by the receiving antenna. In the mono-static configuration the same antenna is used for transmission and reception, while in the bi-static configuration two spatially separate antennas are used. The commonly used terms in a SAR imaging system are defined as,

- ground-range (x): direction orthogonal to the direction of antenna platform motion
- cross-range (y and z): direction parallel to the direction of antenna platform motion
- azimuth (y): direction parallel to the direction of antenna platform motion; for 2D images, this referred to as ‘cross-range’
- elevation (z): direction orthogonal to the plane of azimuth and ground-range
- looking angle (α): direction the antenna beam is pointed, measured against the vertical axis of the antenna
- squint angle (β): direction the antenna beam is pointed, measured against the horizontal axis of the antenna
- beamwidth (θ): range of angles for which the radiation strength is within 3 dB of the maximum strength (half-power beamwidth)
- height: height of the antenna platform
- point spread function (PSF): the reflection received from an ideal point reflector

2.2.2 Resolution

The resolution of a SAR system is measured in terms of the 3 dB pulse width of the point spread function (PSF). The ground-range resolution δ_r is given as [12]

$$\delta_r \approx \frac{c}{2B}, \tag{2.1}$$

where c is the speed of light and B is the bandwidth of the signal. As of (2.1), the ground-rage resolution is inversely proportional to the bandwidth of the signal. Therefore, SAR signals utilize wideband or ultra-wideband pulsed waveforms. The commonly used signal is the *chirp* signal, where the frequency is varied linearly over the pulse duration.

The cross-range resolution (mostly referred to as azimuth resolution) δ_{cr} is given as [12]

$$\delta_{cr} \approx r_0 \frac{\lambda_0}{2L_{\mathrm{SA}}}, \tag{2.2}$$

where r_0 is the distance of the SAR platform to the scene center at closest approach, λ_0 is the wavelength of the signal center frequency and L_{SA} is the length of the synthetic aperture. As of (2.2), the cross-range resolution is inversely proportional to the length of the synthetic aperture. Therefore, as the SAR platform moves, it measures the signal at different positions to create a large effective aperture.

The relationship between L_{SA}, antenna length D, and the beamwidth of the antenna θ is as follows [12]

$$L_{\mathrm{SA}} \approx \frac{\lambda_0 r_0}{D}, \tag{2.3}$$

and

$$\theta \approx \frac{\lambda_0}{D}. \tag{2.4}$$

Substituting for L_{SA} in (2.2), δ_{cr} can be written as

$$\delta_{cr} \approx \frac{\lambda_0}{2\theta}. \tag{2.5}$$

Note that δ_{cr} is also inversely proportional to θ, irrespective of range. Hence a larger antenna beamwidth would improve the cross-range resolution.

The resolution limits discussed here are bounded by the widely used approximated algorithms for image reconstruction (see Section 2.3.2). With the use of computational imaging the resolution can be improved.

2.2.3 SAR Forward Model

As depicted in Fig 2.1, a radar antenna transmits a signal to illuminate the scene within its antenna beamwidth. The scene is comprised of hypothesized point scatters which backscatter the energy, which is then received by the antenna. As the SAR system moves along the trajectory, it obtains measurements of the scene at specified azimuth sampling points. Note that the azimuth sampling distance is chosen to avoid Doppler aliasing [12].

The discrete (sampled) frequency response vector $\mathbf{y}_m$ of the system can be directly measured using specialized equipment (e.g. vector network analyzer). Assuming a scene consisting of N point scatterers, the sampled frequency response $y_{m,l}$, at SAR system position $m \in \{1, \ldots, M\}$ and the l-th frequency sample, where $l \in \{1, \ldots, L\}$, is

$$y_{m,l} = \sum_{n=1}^{N} a_{m,l,n} e^{-j\omega_l \tau_{m,n}} x_n + \nu_{m,l}, \tag{2.6}$$

where x_n is the complex reflection coefficient of the n-th point scatterer, $a_{m,l,n}$ is the path loss and antenna response, ω_l is the angular frequency, $\tau_{m,n}$ is the round-trip time delay between antenna position m and the n-th point scatterer, $\nu_{m,l}$ is the measurement noise, and $j = \sqrt{-1}$. Concatenating all M frequency respose measurements gives

$$\mathbf{y} = \mathbf{H}\mathbf{x} + \boldsymbol{\nu}, \tag{2.7}$$

where $\mathbf{y} = \left[\mathbf{y}_1^T \cdots \mathbf{y}_M^T\right]^T$ is the measurement vector, $\boldsymbol{\nu}$ is the measurement noise, $\mathbf{x} = [x_1, \ldots, x_N]^T$ is the reflectivity vector of the point scatterers, and $(.)^T$ is the transpose operator. The measurement matrix $\mathbf{H}$ gives the dependence between the point scatterers and each measurement. The elements of the measurement matrix are defined as

$$[\mathbf{H}]_{m(L-1)+l,n} = a_{m,l,n} e^{-j\omega_l t_{m,n}}. \tag{2.8}$$

2.3 SAR Image Reconstruction Algorithms

SAR image reconstruction obtains an estimate of the reflection coefficients $\hat{\mathbf{x}}$ from the measurements by solving the inverse problem defined in (2.7). Reconstruction algorithms can be broadly classified into two classes.

1. Inverse filtering
2. Approximation methods

In [4], the authors present a comparison between these two classes (approximation methods are referred to as migration methods). Recently algorithms based on Bayesian frameworks are proposed for SAR image reconstruction. These approaches are mostly developed for sparse signal reconstruction [15, 16, 17, 18], focusing on noise removal and image enhancement.

2.3.1 Inverse Filtering

The solution to (2.7) can be formulated as

$$\hat{\mathbf{x}} = \underset{x}{\operatorname{argmin}} ||\mathbf{y} - \mathbf{H}\mathbf{x}||_2^2, \tag{2.9}$$

which is the least squares solution or the explicit inverse. However, the problem is often ill posed and is computationally complex in both memory and time. The least squares solution is discussed in detail in Section 3.3. Compressive sensing for SAR images has also been developed in the framework of inverse filtering [4].

2.3.2 Approximation Methods

Even though the inverse filtering produces the exact image, due to the heavy computational load traditional SAR image reconstructions are FFT based approximations.

The most widely used algorithm for remote sensing satellite SAR is the range-Doppler algorithm (RDA) which is processed in the domain of range time and azimuth frequency [14]. This process is efficient since the ground-range dimension and cross-range dimension can be separated and the processing can be done separately on each dimension. However, this needs a range cell migration correction and an interpolator is used for this purpose. Hence, approximations are made and the accuracy is limited. Another efficient algorithm is the chirp scaling algorithm (CSA) [14]. Here the interpolation step is eliminated by using chirp scaling and the data is partly processed in the range-Doppler domain and partly processed in the 2D frequency domain. However, if a frequency chirp is not used as the transmitting pulse, the data needs to be expanded with a chirp. One of the accurate algorithms in this category is $\omega - K$ algorithm [14] which process data only in the 2D frequency domain. A problem with processing data in 2D frequency domain is that large changes in average Doppler shift cannot be accommodated (applies to CSA as well). Furthermore, the $\omega - K$ algorithm needs a range frequency interpolation which limits the accuracy.

SAR image reconstruction can be carried out in the time domain as well. Algorithms for finding reflectivity coefficients using time-domain SAR data are known as (convolution) back projection algorithms. Even though this method is accurate, just as in the frequency domain, it has a heavy computational load [19]. Over the years many fast back projection algorithms have been proposed in the literature [20, 21, 22] which include two-stage and multiple-stage back-projection. However, the computational saving is achieved at the expense of image quality and of processing artifacts [20].

Approximation methods can be directly applied to (2.7) by using a matched filter. Here the inverse of $\mathbf{H}$ is approximated by taking the complex conjugate [4]. This solution is stable and robust to noise. Yet, as with other approximations, the achievable resolution is limited. The matched filter is discussed in detail in Section 3.2.

2.4 Dynamic Metasurface Antennas

For spotlight mode SAR and other novel imaging SAR modes proposed in literature [7, 8, 9] beam steering of the radar antennas is required. To achieve beam steering, conventional antennas use mechanically gimbaled antennas [23] or electronically scanned arrays [24]. Even though mechanically gimbaled antennas are electrically less complex, their size, weight and power consumption limits the usage.

Electronically scanned arrays are categorized as passive electronically scanned arrays (PESA) or active electronically scanned arrays (AESA). In PESAs all the elements of the antenna array are connected to a single transmitter/receiver module. The feed signal for each antenna passes through a phase shifter, which controls the direction of the beam. However, since only a single transmitter/receiver pair is used PESA cannot be used to generate complex beam patterns.

In the AESAs, each element of the antenna array is connected to a transmitter/receiver module. Therefore, the gain and the phase can be controlled at each element yielding to complex beam patterns. However, the AESAs hardware architecture is more complex and the power consumption is higher when compared to PESAs .

An alternative are dynamic metasurface antennas (DMA). DMAs are capable of generating frequency and spatially diverse complex beam patterns. It can control amplitude, phase, frequency, polarization of elements of the array, but unlike AESAs there is only one transmitter/receiver module. DMAs use a wave guide, which is connected to subwavelength metasurface unit cells, each of which is able to modulate phase and amplitude. The elements can change the radiation properties to create a dynamic array. DMAs have shown to be a promising approach for SAR imaging [3, 10, 25, 8, 9].

Chapter 3

INVERSE PROBLEM

In this chapter, the inverse problem is introduced. Resolution matrices are discussed as measures of performance. The solution to inverse problems can be approximated (e.g. using a matched filter) or estimated (e.g. using Moore-Penrose pseudo inverse). The advantages and limitations of the two solutions are discussed.

3.1 Defining the Inverse Problem

An inverse problem is the estimation of a set of model parameters from the data which produced them [26]. Let $\mathbf{y}$ be the observed data and $\mathbf{x}$ the model parameters. Then the linear relationship between $\mathbf{y}$ and $\mathbf{x}$ can be modeled as

$$\mathbf{y} = \mathbf{H}\mathbf{x} + \boldsymbol{\nu}, \tag{3.1}$$

where $\mathbf{y} = [y_1 \cdots y_M]^T$ and $\mathbf{x} = [x_1 \cdots x_N]^T$. Here $\boldsymbol{\nu}$ is noise and $(.)^T$ denotes the transpose operator. The length of the observed data (number of measurements), and the number of model parameters is M and N respectively. The forward model developed for SAR image reconstruction in (2.7) is of this form. $\mathbf{H}$ is the measurement matrix (referred to as the design matrix in some literature), which defines the relationship between the observed data and model parameters. The model parameters can be estimated by taking the inverse of (3.1), hence

$$\hat{\mathbf{x}} = \mathbf{H}^{-\mathbf{g}}\mathbf{y}, \tag{3.2}$$

where $\mathbf{H}^{-\mathbf{g}}$ is the generalized inverse of $\mathbf{H}$. In many cases $\mathbf{H}$ is not a full rank matrix and is therefore non-invertible [27]. If $M > N$ the problem is overdetermined, where there is more than necessary information to process the exact solution. For $M < N$ the problem is under-determined and the information is not adequate to determine a unique solution.

To evaluate the performance of the solutions to the inverse problem, resolution matrices can be used. There are two types of resolution matrices, model resolution matrix and data resolution matrix [26].

The model resolution matrix $\mathbf{R}$ defines how well the model parameters can be resolved [26]. Rewriting (3.2) by inserting (3.1) gives

$$\hat{\mathbf{x}} = \mathbf{H}^{-\mathbf{g}}(\mathbf{H}\mathbf{x} + \boldsymbol{\nu}) \tag{3.3}$$

$$= \mathbf{H}^{-\mathbf{g}}\mathbf{H}\mathbf{x} + \mathbf{H}^{-\mathbf{g}}\boldsymbol{\nu}. \tag{3.4}$$

Hence, $\mathbf{R}$ is defined as

$$\mathbf{R} = \mathbf{H}^{-\mathbf{g}}\mathbf{H}. \tag{3.5}$$

If the model parameters can be perfectly resolved, $\mathbf{R}$ converges to an identity matrix.

The data resolution matrix $\mathbf{N}$ defines how well the estimated parameters fit the measured data [26]. Using (3.2) $\mathbf{y}$ can be predicted as

$$\mathbf{y}^{pre} = \mathbf{H}\mathbf{H}^{-\mathbf{g}}\mathbf{y}. \tag{3.6}$$

Then $\mathbf{N}$ is defined as

$$\mathbf{N} = \mathbf{H}\mathbf{H}^{-\mathbf{g}}. \tag{3.7}$$

As before, if the estimated parameters fit the data perfectly, $\mathbf{N}$ converges to an identity matrix.

As the resolution matrix ideally converges to an identity matrix, a possible metric to measure the performance of the resolution matrix is the spread of off diagonal elements. This is known as the *Dirichlet spread function* [26]. The spread of the model resolution matrix is given as

$$\text{spread}\,\{\mathbf{R}\} = ||\mathbf{R} - \mathbf{I}||_2^2 = \sum_{i=1}^{N}\sum_{j=1}^{N}[[\mathbf{R}]_{i,j} - [\mathbf{I}]_{i,j}]^2. \tag{3.8}$$

The spread of the data resolution matrix is given as

$$\text{spread}\,\{\mathbf{N}\} = ||\mathbf{N} - \mathbf{I}||_2^2 = \sum_{i=1}^{M}\sum_{j=1}^{M}[[\mathbf{N}]_{i,j} - [\mathbf{I}]_{i,j}]^2. \tag{3.9}$$

The spread calculates the L_2 norm of the difference between the identity matrix and the resolution matrix. When the resolution matrix converges to the identity matrix, the spread converges to zero.

3.2 Approximating the Inverse

Since $\mathbf{H}$ is often not invertible, an alternative is to approximate the inverse. One of the most widely used approximation methods is the matched filter [4].

In the matched filter solution, the inverse is approximated by the adjoint operator, thus

$$\mathbf{H}^{-g} = \mathbf{H}^*, \tag{3.10}$$

where $(.)^*$ is the complex conjugate transpose operator. The resolution matrices are

$$\mathbf{R}_{\text{MF}} = \mathbf{H}^*\mathbf{H}, \tag{3.11}$$

and

$$\mathbf{N}_{\text{MF}} = \mathbf{H}\mathbf{H}^*. \tag{3.12}$$

The matched filter solution is stable and robust to noise. However, the achievable resolution is limited [4].

3.3 Least Squares Solution

The least squares solution is useful when there is no exact solution to the inverse problem. The idea behind the least squares solution is to minimize the squares of the residual error.

For an overdetermined problem, the inverse can be estimated using the least squares solution as

$$\mathbf{H}^{-g} = (\mathbf{H}^{*}\mathbf{H})^{-\mathbf{1}}\mathbf{H}^{*}, \tag{3.13}$$

with the resolution matrices

$$\mathbf{R}_{\mathrm{LS}} = (\mathbf{H}^{*}\mathbf{H})^{-\mathbf{1}}\mathbf{H}^{*}\mathbf{H}, \tag{3.14}$$

and

$$\mathbf{N}_{\mathrm{LS}} = \mathbf{H}(\mathbf{H}^{*}\mathbf{H})^{-\mathbf{1}}\mathbf{H}. \tag{3.15}$$

Note that model resolution matrix $\mathbf{R}_{\mathrm{LS}}$ is an identity matrix, and hence, the parameters can be perfectly resolved.

However, in the case of inadequate information, the least squares solution fails as $(\mathbf{H}^{*}\mathbf{H})^{-\mathbf{1}}$ does not exist for an underdetermined problem. A way to obtain an estimate is to use prior information. A fundamental prior assumption is that the solution is *simple* [26], where the simplicity is characterized by the Euclidean length (L_2 norm) of the solution. Hence, the problem can be reformulated as follows: Find $\hat{\mathbf{x}}$ such that $||\hat{x}||^2$ is minimized subject to the constraint $||\mathbf{y} - \mathbf{H}\mathbf{x}||_2^2 = 0$.

This is referred to as the minimum norm solution (minimum length) and can be solved using Lagrange multipliers. In this case, the inverse is estimated as

$$\mathbf{H}^{-g} = \mathbf{H}^{*}(\mathbf{H}^{*}\mathbf{H})^{-\mathbf{1}}. \tag{3.16}$$

For the minimum norm solution, the resolution matrices are

$$\mathbf{R}_{\mathrm{MN}} = \mathbf{H}^*(\mathbf{H}\mathbf{H}^*)^{\mathbf{-1}}\mathbf{H}, \tag{3.17}$$

and

$$\mathbf{N}_{\mathrm{MN}} = \mathbf{H}\mathbf{H}^*(\mathbf{H}\mathbf{H}^*)^{\mathbf{-1}}. \tag{3.18}$$

In contrast to the over determined case, now the data resolution matrix $\mathbf{N}_{\mathrm{MN}}$ is an identity matrix. Hence there exists a possibility that the model parameters are not perfectly resolved. However, the estimated parameters would perfectly fit the measured data.

3.3.1 Moore Penrose Pseudo Inverse

The Moore Penrose pseudo inverse essentially gives the same two solutions as least squares and minimum norm [28]. Let $\mathbf{H}$ be a matrix of size $M \times N$. Then the pseudo inverse $\mathbf{H}^\dagger$ of $\mathbf{H}$ is computed as follows: If $\mathbf{H}$ has linearly independent columns ($M > N$), $\mathbf{H}^\dagger = (\mathbf{H}^*\mathbf{H})^{\mathbf{-1}}\mathbf{H}^*$. This is called the left inverse. If $\mathbf{H}$ has linearly independent rows ($M < N$), $\mathbf{H}^\dagger = \mathbf{H}^*(\mathbf{H}^*\mathbf{H})^{\mathbf{-1}}$. This is called the right inverse.

3.3.2 Singular Value Decomposition (SVD)

The Moore Penrose pseudo inverse (both left inverse and right inverse) can be computed by using *singular value decomposition (SVD).* Here the matrix $\mathbf{H}$ can be decomposed as

$$\mathbf{H} = \mathbf{U}\mathbf{\Sigma}\mathbf{V}^*, \tag{3.19}$$

where the column vectors $\mathbf{v}$ of $\mathbf{V}$ are called right singular vectors, and the column vectors $\mathbf{u}$ of $\mathbf{U}$ are called left singular vectors. The singular values are complex positive valued numbers and are typically ordered in descending order in the diagonal matrix $\mathbf{\Sigma}$.

The pseudoinverse is formulated using the singular vectors and the singular values as

$$\mathbf{H}^{\dagger} = \mathbf{V}\mathbf{\Sigma}^{-\mathbf{1}}\mathbf{U}^{*}. \tag{3.20}$$

A bad condition number, indicating that there exist singular values that are small compared to the rest, causes the inverse to be unstable and the problem to be ill-conditioned. Therefore, small singular values need to be discarded, and this can be used as a form of a regularizer, namely truncated singular value decomposition (TSVD). However, this truncation degrades the resolution (see Section 3.4).

Another disadvantage of the pseudo inverse solution is that it is computationally complex in both memory and time. In many cases, with a large matrix **H**, it is not feasible to find $\mathbf{H}^{\dagger}$ with the hardware constraints of standard PCs.

3.4 Regularizing the Inverse Problem

3.4.1 Truncated Singular Value Decomposition (TSVD)

There are several reguralizers proposed in literature such as Tikohonov regularization [29], L_1 norm [30] and total variation (TV) norm [28]. In this work, truncated singular value decomposition (TSVD) is used as the regularizer [28], since SVD is used to compute the pseudo inverse.

In TSVD, singular values near zero are discarded as they cause the inverse to be unstable and the problem to be ill-conditioned. If t singular values are retained, $\mathbf{H}^{\dagger}$ can be formulated as

$$\mathbf{H}^{\dagger} = \mathbf{V}_t\mathbf{\Sigma}_t^{-1}\mathbf{U}_t^{*}, \tag{3.21}$$

where $\mathbf{U}_t$ and $\mathbf{V}_t$ consists of the first t columns of the respective matrices. The resolution matrices are now formulated as [26]

$$\mathbf{R} = \mathbf{V}_t \mathbf{V}_t^*, \tag{3.22}$$

and

$$\mathbf{N} = \mathbf{U}_t \mathbf{U}_t^*. \tag{3.23}$$

From (3.22), the model parameters will be perfectly resolved if $\mathbf{V}_t$ spans the parameter space (if $t \geq M$ and eigenvalues are non-zero).

Thus, if more singular values are kept the accuracy of the inverse will improve, but if some singular values are small compared to the rest, the system will be unstable and more sensitive to noise. If only a low number of singular values are kept, noise can be mitigated, but information will be lost in the process (yielding regularization errors [31]). Hence, an optimal truncation point needs to be found.

3.4.2 Optimal regularization

There are several methods proposed in the literature to find the optimal truncation point. These include the unbiased predictive risk estimator, the discrepancy principle, the generalized cross validation, and the L-curve method [28]. In this work the L-curve method is used as it is more robust in the presence of correlated errors and does not need prior information about the errors. The L-curve is a parametric plot of the norm of the regularized solution $\hat{\mathbf{x}}$ versus the norm of the corresponding residual $\mathbf{H}\hat{\mathbf{x}} - \mathbf{y}$ [31]. The corner of the L-curve corresponds to a good balance between the minimization of the norm of the solution, and the norm of the corresponding residuals. At this point the solution changes from being dominated by regularization errors to being dominated by noise.

Chapter 4

PARTITIONED INVERSE IMAGE RECONSTRUCTION ALGORITHM

In this chapter, the partitioned inverse algorithm for SAR image reconstruction is introduced. The proposed algorithm avoids the time and memory constrains of the generalized inverse while maintaining the improved resolution. Here the algorithm is introduced, and the mathematical model developed and analyzed using resolution matrices and point spread functions.

Some content of this chapter is based on a previous work of the author [5].

4.1 Model of the Partitioned Reconstruction

As discussed in Chapter 2, SAR image reconstruction is a computationally complex inverse problem. To handle the large set of data and the computational hardware constraints, the proposed algorithm partitions the reconstruction. The partitioning is two-fold and done according to the geometry shown in Fig. 2.1.

Step 1: Partitioning of the measurement vector into sub-apertures $\{\mathbf{y}_m\}$ by the SAR system position:

$$\mathbf{y}_m = [y_{m,1}, \ldots, y_{m,L}]^T. \tag{4.1}$$

Step 2: Partitioning the reconstruction scene as observed by the 3 dB beamwidth of the antenna at each position:

$$\tilde{\mathbf{x}}_m = [x_{m,1}, \ldots, x_{m,N'}]^T, \tag{4.2}$$

where $N^{'} << N$ is the number of point scatterers observed by the antenna at each position. The relationship between $\tilde{\mathbf{x}}_m$ and $\mathbf{x}$ can be formulated as,

$$\tilde{\mathbf{x}}_m = \mathbf{J}_m \mathbf{x}. \tag{4.3}$$

For the 2D imaging case (see Fig. 2.1a), the boundaries of the partitioned scene are

$$y_{\text{lb}} = y + \frac{h}{\cos\alpha}\tan\beta - \frac{h}{\cos\alpha}\tan(\frac{\theta_y}{2}), \tag{4.4}$$

for the lower azimuth bound, and

$$y_{\text{ub}} = y + \frac{h}{\cos\alpha}\tan\beta + \frac{h}{\cos\alpha}\tan(\frac{\theta_y}{2}), \tag{4.5}$$

for the upper azimuth bound. For the 3D imaging case (see Fig. 2.1b), the boundaries of the partitioned scene are

$$y_{\text{lb}} = y + r\tan\beta - \frac{r}{\cos(90-\alpha)}\tan(\frac{\theta_y}{2}), \tag{4.6}$$

for the lower azimuth bound,

$$y_{\text{ub}} = y + r\tan\beta + \frac{r}{\cos(90-\alpha)}\tan(\frac{\theta_y}{2}), \tag{4.7}$$

for the upper azimuth bound,

$$z_{\text{lb}} = z + r\tan(90-\alpha) - \frac{r}{\cos(90-\alpha)}\tan(\frac{\theta_z}{2}), \tag{4.8}$$

for the lower elevation bound, and

$$z_{\mathrm{ub}} = z + r\tan(90-\alpha) + \frac{r}{\cos(90-\alpha)}\tan(\frac{\theta_z}{2}), \tag{4.9}$$

for the upper elevation bound. Here r represents the maximum ground-range and θ_y and θ_z denotes the 3 dB beamwidth in azimuth and elevation, respectively. Note that Fig. 2.1b depicts a beam, where α is fixed to 90^0 and β is fixed to 0^0.

Here the contributions of point scatterers outside of the 3 dB antenna beamwidth are not considered in the forward model. Although this inevitably results in model residuals, validation measurements (as presented in Chapter 5) suggest that this error is insignificant and can be neglected.

The model for partition m can be formulated as

$$\mathbf{y}_m = \mathbf{H}_m\tilde{\mathbf{x}}_m + \boldsymbol{\nu}_m. \tag{4.10}$$

Here $\mathbf{H}_m$ is a $L \times N'$ matrix, which is much smaller than the size of the original $(ML) \times N$ measurement matrix. Instead of obtaining the inverse of the full measurement matrix, this approach computes the inverse of the sub-measurement matrices and solves for each sub-aperture separately.

An added advantage of such a partition is that the sub-measurement matrix $\mathbf{H}_m$ is constant for all the partitions in the stripmap mode. Defining $\mathbf{H}_{\mathrm{s}}$ as the constant sub-measurement matrix, $\mathbf{H}_m = \mathbf{H}_{\mathrm{s}}\ \forall\ m \in \{1, \dots, M\}$. As of (2.8), the variables in the measurement matrix are the frequencies $\{\omega_l\}$ and time delays $\{\tau_{m,n}\}$. The frequency samples remain the same for each system position, and by translating the fixed reconstruction volume for each position the time delays also remain constant. Therefore, construction of the sub-measurement matrix and its inversion need to be done only once. This potentially saves a lot of memory and computation time.

As the measurements and reconstruction points are partitioned for each SAR position, the system model can be rearranged to give

$$\mathbf{y} = \tilde{\mathbf{H}}\tilde{\mathbf{x}} + \boldsymbol{\nu}, \tag{4.11}$$

where $\tilde{\mathbf{x}} = [\tilde{\mathbf{x}}_1^T \cdots \tilde{\mathbf{x}}_M^T]^T$, and the rearranged measurement matrix

$$\tilde{\mathbf{H}} = \begin{bmatrix} \mathbf{H}_\mathrm{s} & \mathbf{0} & \cdots \\ \mathbf{0} & \ddots & \\ \vdots & & \end{bmatrix}. \tag{4.12}$$

As seen in (4.12), $\tilde{\mathbf{H}}$ is a block diagonal matrix. The inverse is given as

$$\hat{\mathbf{x}} = \mathbf{W}\tilde{\mathbf{H}}^{-g}\mathbf{y}, \tag{4.13}$$

where $\mathbf{W}$ is a weighted summation matrix defined as $\mathbf{W} = \begin{bmatrix} \mathbf{W}_1 & \cdots \mathbf{W}_M \end{bmatrix}$, with $\sum_m^M \mathbf{W}_m\mathbf{J}_m = \mathbf{I}$. The weighing matrix $\mathbf{W}$ coherently sums and rearranges the elements in $\tilde{\mathbf{H}}^{-g}\mathbf{y}$ to coincide with the cordinates of the actual scene, and $\tilde{\mathbf{H}}^{-g}$ is defined as

$$\tilde{\mathbf{H}}^{-g} = \begin{bmatrix} \mathbf{H}_\mathrm{s}^{-g} & \mathbf{0} & \cdots \\ \mathbf{0} & \ddots & \\ \vdots & & \end{bmatrix}. \tag{4.14}$$

$\mathbf{H}_\mathrm{s}^{-g}$ can be estimated by the matched filter (Section 3.2) or the pseudo inverse (Section 3.3). For the partitioned matched filter (PMF), (4.14) is given as

$$\tilde{\mathbf{H}}^{-g} = \begin{bmatrix} \mathbf{H}_\mathrm{s}^{*} & \mathbf{0} & \cdots \\ \mathbf{0} & \ddots & \\ \vdots & & \end{bmatrix}. \tag{4.15}$$

For the partitioned pseudo inverse (PPI), (4.14) is given as

$$\tilde{\mathbf{H}}^{-g} = \begin{bmatrix} \mathbf{H}_{\mathrm{s}}^{\dagger} & \mathbf{0} & \cdots \\ \mathbf{0} & \ddots & \\ \vdots & & \end{bmatrix}. \tag{4.16}$$

To formulate the model resolution, $\tilde{\mathbf{x}}$ is written in terms of $\mathbf{x}$ as

$$\tilde{\mathbf{x}} = \mathbf{J}\mathbf{x}, \tag{4.17}$$

where $\mathbf{J} = \begin{bmatrix} \mathbf{J}_1 & \cdots \mathbf{J}_M \end{bmatrix}^T$.

Combining (4.11) and (4.13) the estimate can be formulated as

$$\hat{\mathbf{x}} = \mathbf{W}\tilde{\mathbf{H}}^{-g}(\tilde{\mathbf{H}}\mathbf{J}\mathbf{x} + \boldsymbol{\nu}). \tag{4.18}$$

Hence, the model resolution can be formulated as

$$\mathbf{R}_{\mathbf{PI}} = \mathbf{W}\tilde{\mathbf{H}}^{-g}\tilde{\mathbf{H}}\mathbf{J}. \tag{4.19}$$

Note that when $\mathbf{H}_{\mathrm{s}}^{\dagger}$ is an overdetermined least squares problem, $\mathbf{R}_{\mathbf{PI}}$ is an identity matrix.

The Predicted values of the data is given as

$$\mathbf{y}^{\mathbf{pre}} = \tilde{\mathbf{H}}\tilde{\mathbf{H}}^{-g}\mathbf{y}, \tag{4.20}$$

hence, the data resolution can be formulated as

$$\mathbf{N}_{\mathbf{PI}} = \tilde{\mathbf{H}}\tilde{\mathbf{H}}^{-g}. \tag{4.21}$$

Note that when $\mathbf{H}_{\mathrm{s}}^{\dagger}$ is an underdetermined minimum norm problem, $\mathbf{N}_{\mathbf{PI}}$ is an identity matrix.

4.2 Performance Evaluation

In this section, the algorithm is analyzed using results based on synthesized data for the full pseudo inverse (FPI), matched filter (MF), partitioned matched filter (PMF) and partitioned pseudo inverse (PPI). The simulation setup assumes a horn antenna with a half power beamwidth of 58°. The antenna is moved over 0.10 m at intervals of 4 mm, with a looking angle of 30° and a platform height of 0.3 m. The squint angle is fixed at zero. Frequencies from 20 GHz to 26 GHz are used with a sampling interval of 60 MHz (101 values). The scene to be reconstructed is 0.2 m in ground-range and 0.484 m in azimuth. These values were chosen to make reconstruction using FPI possible on the workstation used (Intel Core i7-6700 CPU at 3.4 GHz with 16 GB memory).

4.2.1 Regularization

The sub-measurement matrix is ill-conditioned and needs to be regularized in order to compute the pseudo inverse. Truncated singular value decomposition (TSVD) and L-curves (discussed in Section 3.4) are chosen to regularize the partitioned sub-problems and to find the optimal truncation point. With different noise levels, the amount of regularization changes. In Fig. 4.1, L-curves for PPI with various SNR values are shown. The corner points of the L-curves represent the optimal truncation point for the respective noise levels; 30 dB SNR: 17 points, 20 dB SNR: 15 points, 10 dB SNR: 13 points and 0 dB SNR: 11 points. As the noise level increases, the norm of the residuals also increases.

4.2.2 Resolution Matrix

As discussed in Section 3.1, the model resolution spread is a possible metric to measure the resolution of the parameters. The model resolution spread of MF, PMF, FPI and PPI are

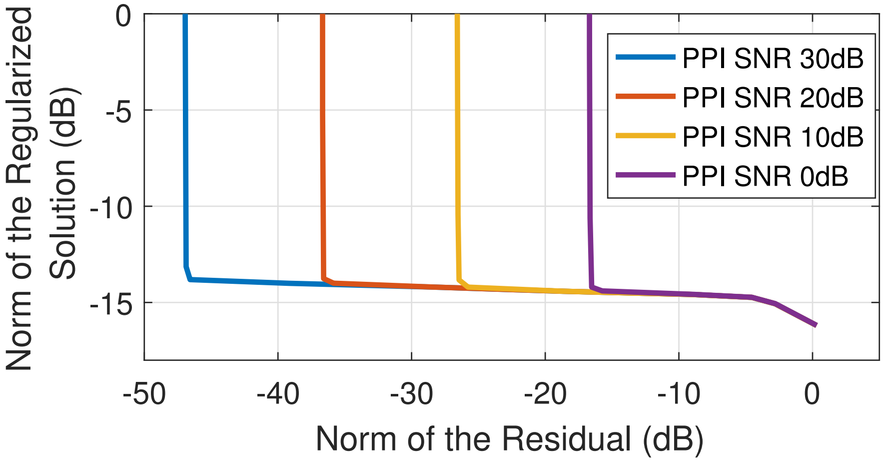

Figure 4.1: L-curves plotted for different noise levels.

investigated against the number of singular values retained and shown in Fig. 4.2. If the value of the model resolution spread is zero, the point sources are perfectly resolved.

The values are normalized using the norm of $\mathbf{I}$. The maximum number of singular values retained is 101, as that is the minimum size of $\mathbf{H}_s$. The resolution spread of FPI and PPI changes with the amount of truncation, and at 101 points it is 0.9919 and 0.9789 respectively. The resolution spread of MF and PMF is 0.9984 and 1 respectively, and are near the lower bound of both FPI and PPI. There is an improvement of 2% and 1.3% in the resolution spread in PPI over MF and FPI respectively, at 101 points.

For PPI, the number of reconstruction points is less than for FPI. Therefore, when a small number of singular values are kept, resolution spread is better for PPI than for FPI. Furthermore, for PPI only the points in the partitioned scene affect the estimate, and most of the off diagonal elements in the model resolution matrix are zero.

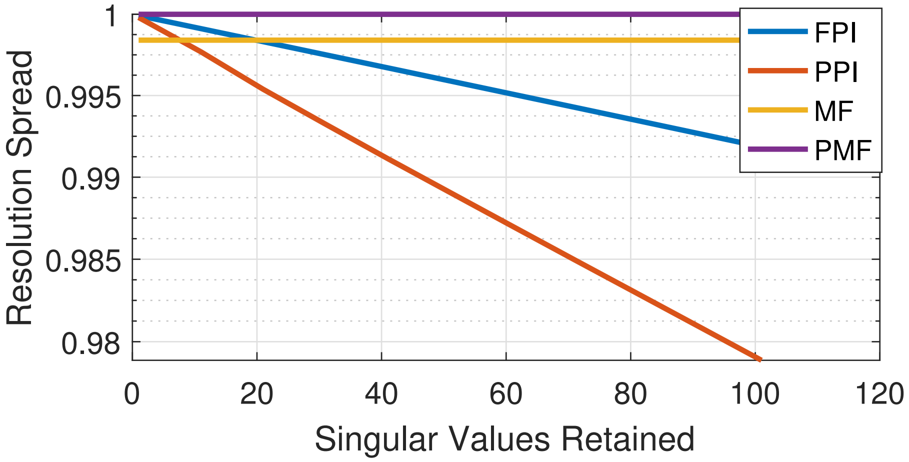

Figure 4.2: Model resolution spread plotted against the number of singular values retained.

4.2.3 Point Spread Function (PSF)

Figs. 4.3a and 4.3b demonstrate the effect of different noise levels for a PSF of PPI with a fixed truncation of 15 points. For signals with 0 dB and 10 dB SNR, the point scatterer is not resolvable. For signals with lower noise levels, the resolution of the PSF is 1.87 cm in ground-range and 2.38 cm in cross-range. The resolution values remain the same across all noise levels as the truncation point is fixed.

PSFs of PPI, using optimal truncation points for different noise levels are shown in Figs. 4.4a and 4.4b. As the resolution depends on the amount of truncation, different resolutions can be observed as noise levels vary. In an ideal case with no noise, the PSF of PPI is a peak as there is no truncation. When the noise level increases, the resolution degrades. This is clearly visible in Fig. 4.4a, with the ground-range resolution for respective noise levels being, 0 dB SNR: 2.36 cm, 10 dB SNR: 2.09 cm, 20 dB SNR: 1.86 cm, and 30 dB SNR: 1.69 cm. However, as the cross-range data is limited, there is no visible degradation

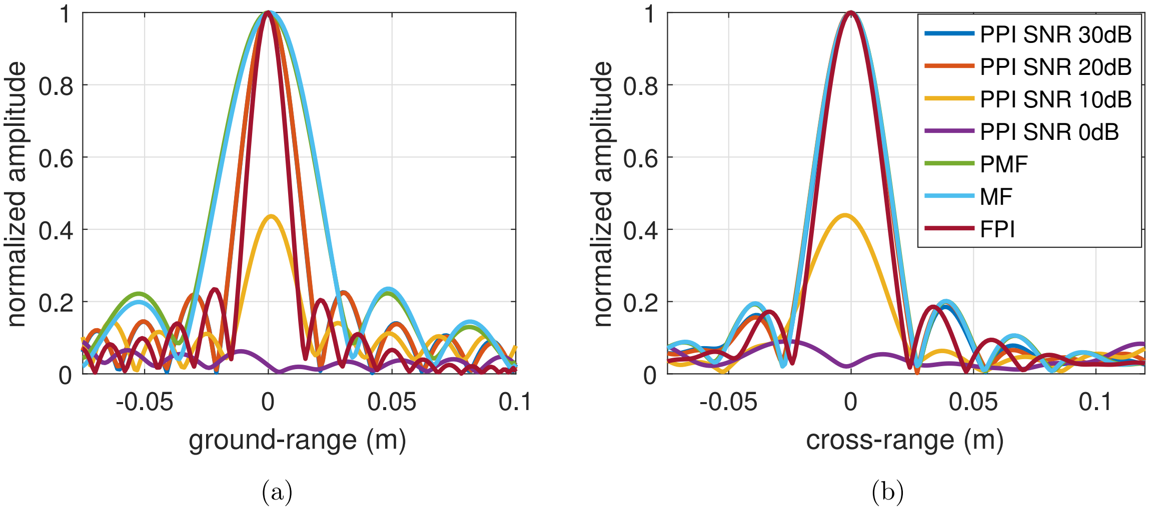

Figure 4.3: Effect of noise: (a) ground-range profile of the PSF with a fixed truncation of 15, (b) cross-range profile of the PSF with a fixed truncation of 15.

of resolution in Fig. 4.4b, where the cross-range resolution is 2.38 cm across all noise levels. This suggests that the PPI method is robust to noise.

For comparison, the PSF with MF, PMF and FPI under ideal conditions are shown in Figs. 4.3 and 4.4. Resolution with MF and PMF is 3.10 cm in ground-range and 2.40 cm in cross-range, while resolution with FPI is 1.33 cm and 2.07 cm respectively. When computing the FPI, the default truncation level computed by MATLAB (506) was used, and thus a good resolution was achieved. However, even for 0 dB SNR, the resolution has improved by 24% in ground-range and 0.83% in cross-range for PPI over MF.

For a reconstruction of the PSF, PMF took 0.97 s, PPI 1.9 s, MF 7.2 s and FPI 2200 s, making PPI 1200 times faster than FPI and 4 times faster than MF. Even though PMF is faster, the computation of sub-measurement matrix and its inversion can be done off-line,

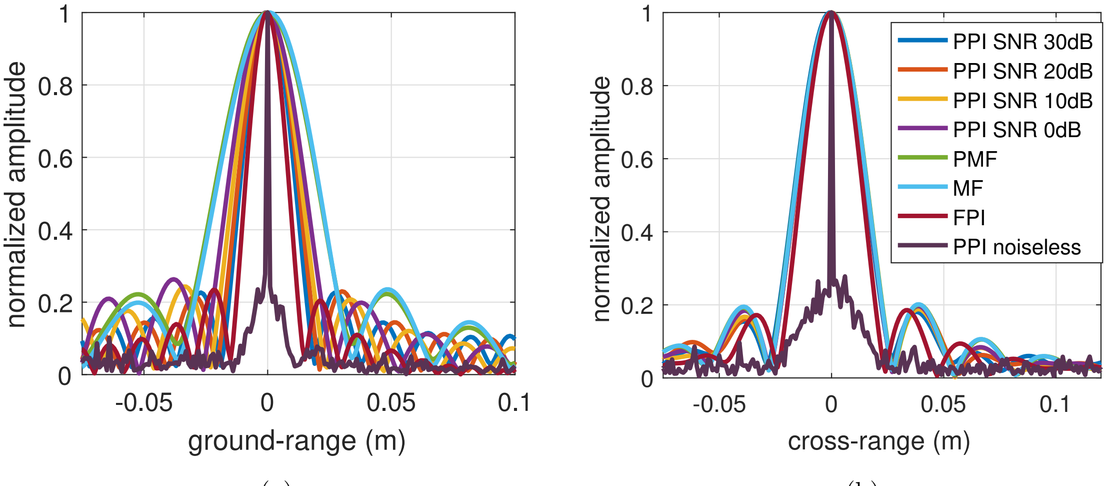

(a) (b)

Figure 4.4: Effect of noise: (a) ground-range profile of the PSF with optimal truncation, (b) cross-range profile of the PSF with optimal truncation.

making PPI just as efficient as PMF.

4.2.4 Aliasing with PI

A drawback of the PI approach is that if the reconstruction scene in the cross-range is sampled at a lower rate, aliasing can occur. The reconstruction sampling interval needs to be smaller than the alias-free measurement sampling interval (in azimuth direction).

As seen in Fig. 4.5, the aliasing pattern is similar to a reconstruction with the measurement sampling rate below the Nyquist sampling rate. Fig. 4.5 is based on synthesized data for a point source, where the Nyquist sampling interval is 8 mm. Fig. 4.5a is the result of PMF reconstruction, when the measurement sampling interval is 1 mm, and the reconstruction sampling interval is 8 mm. This is the expected result. In Fig. 4.5b, the measurement

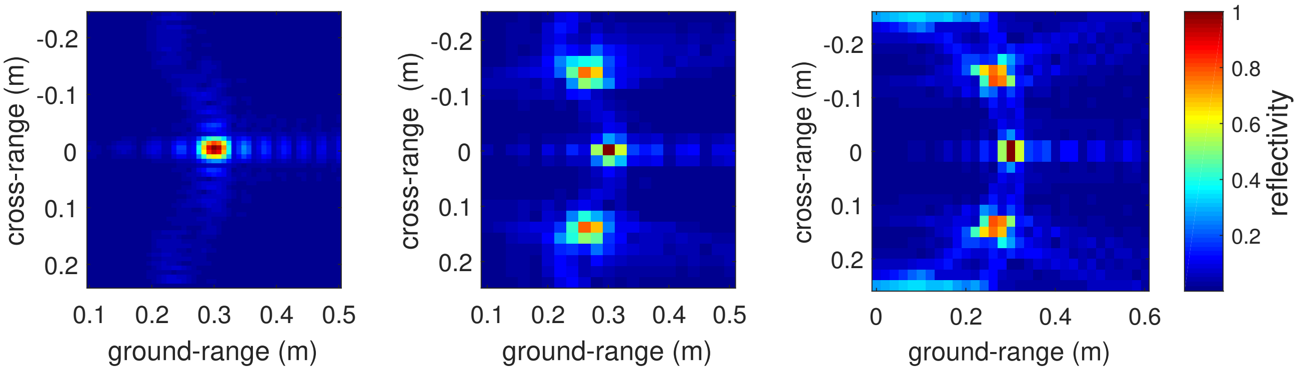

(a)

(b)

(c)

Figure 4.5: Aliasing in PI: (a) PMF reconstruction with 8 mm reconstruction sampling interval, (b) PMF reconstruction with 2 cm reconstruction sampling interval, (c) MF reconstruction with 2 cm measurement sampling interval.

sampling interval is kept as 1 mm, but the reconstruction sampling interval is 2 cm. The reconstruction is done using PMF and the aliasing effect is visible. The aliasing pattern is similar to Fig. 4.5c, where the measurement sampling interval is 2 cm and the reconstruction is done using MF.

This aliasing phenomenon happens because the results from the partitioned reconstructions are summed up. When the reconstruction sampling interval is high, the partitions overlap at several points creating aliasing.

Figs. 4.6 and 4.7 illustrates the results from individual partitions for reconstruction done using PMF. Individual results have only the ground-range information. Figs. 4.6a, 4.6b and 4.6c are results from partitions numbered 1, 50, and 100 respectively when the reconstruction sampling interval is 2 mm. Figs. 4.7a, 4.7b and 4.7c are results from partitions

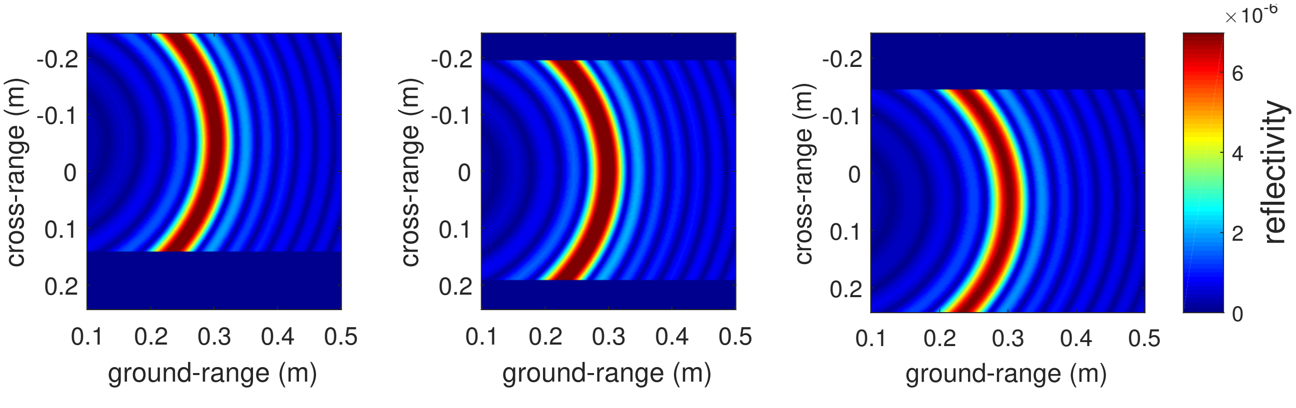

(a) (b) (c)

Figure 4.6: Results from seperate partitions with the reconstruction sampling interval being 2 mm: (a) 1^{st} partition, (b) 50^{th} partition,(C) 100^{th} partition.

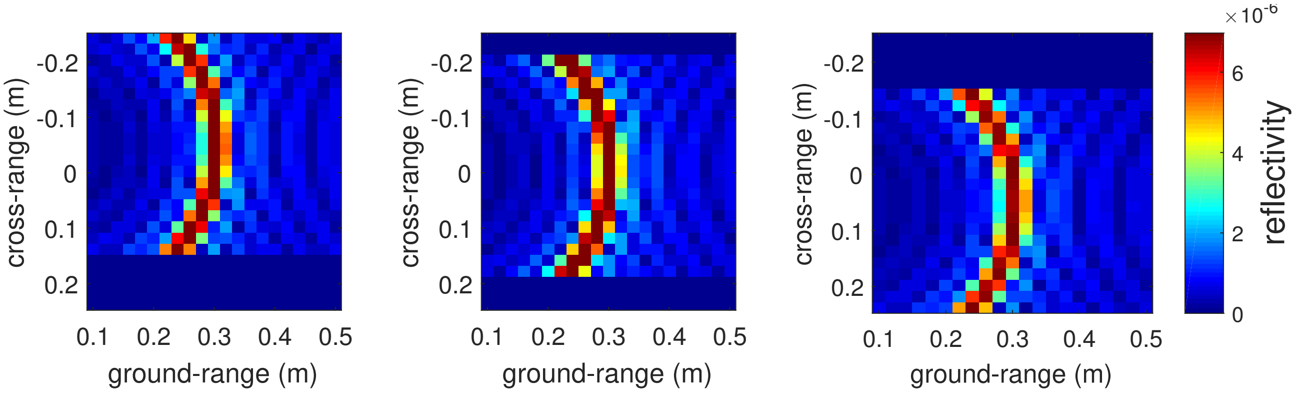

(a) (b) (c)

Figure 4.7: Results from seperate partitions with the reconstruction sampling interval being 2 cm: (a) 1^{st} partition, (b) 50^{th} partition,(C) 100^{th} partition.

numbered 1, 50, and 100 respectively when the reconstruction sampling interval is 2 cm. With the coarser reconstruction sampling interval, many pixels start to overlap.

However, this will not cause practical problems as PI algorithms are proposed for high resolution images, where the reconstruction sampling rate is expected to be high.

Chapter 5

GPU ACCELERATED PARTITIONED INVERSE ALGORITHM

In this chapter experimental results using a laboratory K-Band (15-26.5 GHz) ultra-wideband SAR system are presented to validate the PI algorithm. 2D imaging results and 3D imaging results are presented. As the proposed method allows for parallel processing, a graphic processing unit (GPU) is utilized to achieve a dramatic speedup.

Some content of this chapter is based on the previous work of the author [5, 6].

5.1 Implementation

Since $\tilde{\mathbf{H}}^{-g}$ in (4.13) is a block diagonal matrix, it can be solved in parallel. The weighted summation matrix $\mathbf{W}$ can be partitioned as follows.

$$\mathbf{W} = \left[\begin{array}{cc} \mathbf{W}_1 & \cdots \mathbf{W}_M \end{array} \right]. \tag{5.1}$$

Hence $\hat{\mathbf{x}}$ can be estimated as

$$\hat{\mathbf{x}} = \sum_{m=1}^{M} \mathbf{W}_m \mathbf{H}_{\mathrm{s}}^{-g} \mathbf{y}_m. \tag{5.2}$$

Fig. 5.1 illustrates a block diagram of the parallel implementation. A graphic processing unit (GPU) can be utilized to implement the algorithm.

5.2 2D Imaging Results

In this section, experimental results using two Pasternack PE9852/2F-10 K-band horn antennas with a half power beamwidth of 58° used in a bi-static configuration are presented. The

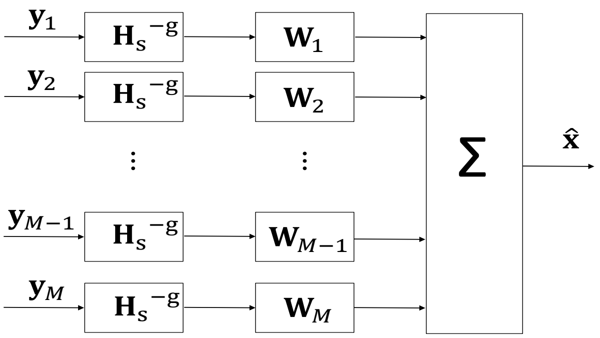

Figure 5.1: Block diagram of the implemented algorithm.

antennas are moved 0.57 m at a spacing of 4 mm and a looking angle of 60° on a platform at a height of 0.3 m. The squint angle is fixed at zero. Frequencies from 15 GHz to 26.5 GHz are used, spaced at 50 MHz intervals. At each antenna position, transfer function measurements are collected using an Agilent A5222N vector network analyzer. The reconstruction scene is 0.6 m in ground-range and 1.1 m in cross-range (azimuth in this example). The azimuth dimension was chosen to reconstruct the scene as observed by all antenna positions. The spacing between voxels is 1 mm. A circle of point scatterers consisting of eighteen 1/4”–20 nuts comprises the scene to be imaged. The nuts were placed equidistantly on a circle of 13 cm in diameter. The reconstruction was performed in MATLAB.

Reconstructed images using MF, PMF and PPI are shown in Figs. 5.2b-5.2d, respectively, where reflectivity is normalized and represented on a logarithmic scale. Reconstructions were done using a Intel Core i7-6700 CPU at 3.4 GHz with 16 GB memory. Reconstruction using FPI was not possible with the available memory. The reconstructed images using MF and

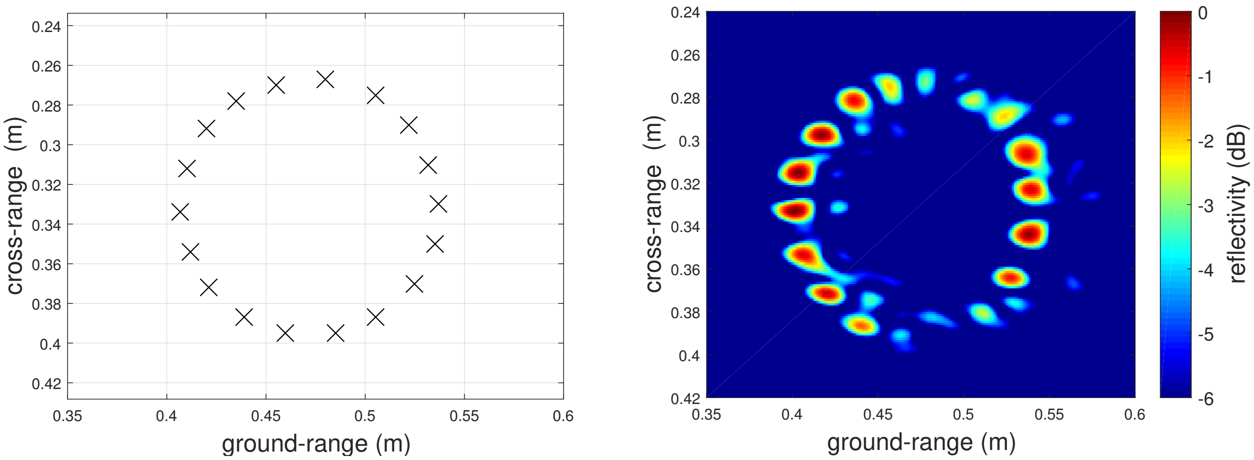

(a) scene

(b) MF

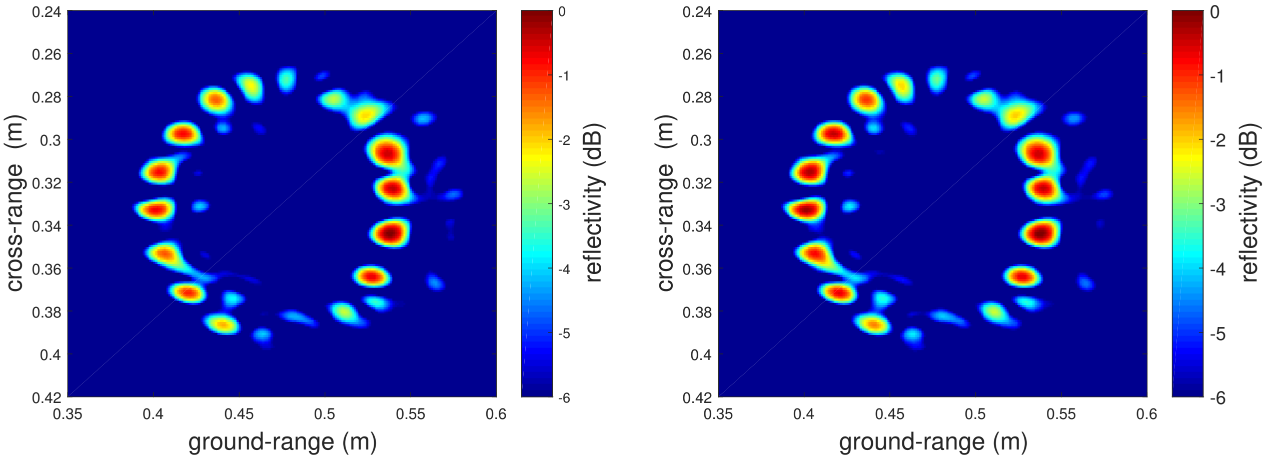

(c) PMF

(d) PPI

Figure 5.2: Experimental results of 2D imaging: (a) positions of point targets, (b) MF reconstruction, (c) PMF reconstruction, (d) PPI reconstruction (36 singular values retained).

PI algorithms show essentially no visible difference, demonstrating that PI works amidst real measurement noise. Reconstruction using MF took 230 s while PMF and PPI took only 20 s and 29 s respectively, making PI 11 times faster on the used workstation.

5.3 3D Imaging Results

In this section, 3D SAR images from a laboratory experiment are presented. Two Pasternack PE9852/2F-10 K-band horn antennas with a half power beamwidth of 58° are used in a bi-static configuration. The antenna platform is moved 0.6 m in azimuth (y) and 0.6 m in elevation (z) at a spacing of 4 mm. The looking angle is 90° and the squint angle is 0°. Frequencies from 15 GHz to 26.5 GHz are used, spaced at 200 MHz intervals. At each antenna position, transfer function measurements are collected using an Agilent A5222N vector network analyzer. The scene as observed by all antenna positions is 0.2 m in ground-range, 1.252 m in azimuth and 1.256 m in elevation. The scene is a metal coated toy balloon dog, as shown in Fig. 5.3a. The reconstruction was performed in MATLAB.

Reconstructed images using MF, PMF, and PPI are shown in Figs. 5.3b, 5.3c, 5.3d, respectively, where the reflectivity is normalized and represented on a logarithmic scale. The images consist of 4,914,100 voxels, each with a voxel spacing of 4 mm. As with the earlier example, reconstruction using FPI was not possible with the available memory. The optimal number of singular values to be retained in PPI was found to be 23. The PPI solution shows essentially no visible difference when compared with the MF and has visibly less clutter than the PMF.

Table 1 shows the time taken to reconstruct the 3D image using different algorithms. A NVIDIA GeForce GTX 960 GPU with 4 GB memory has been used to accelerate the computation. The reconstruction with GPU acceleration took 41 s and 50 s with the PMF and PPI, respectively. This timing includes the construction of the sub-measurement ma-

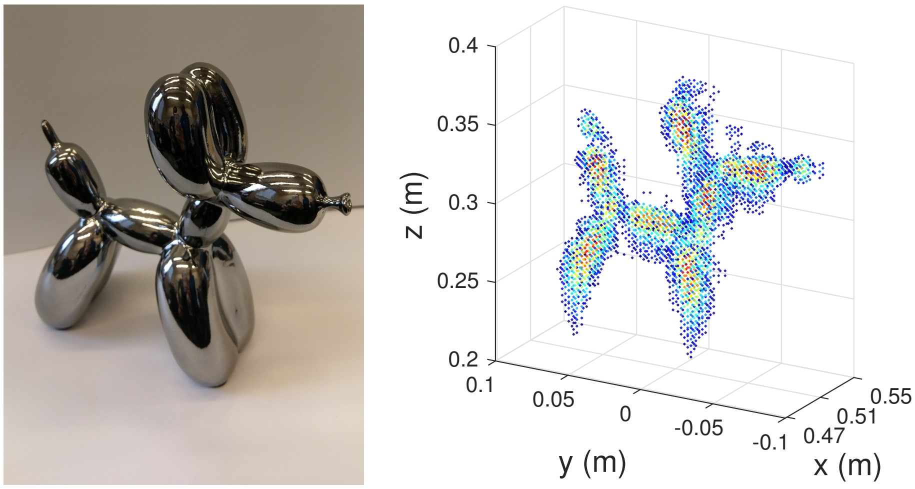

(a) scene (b) MF

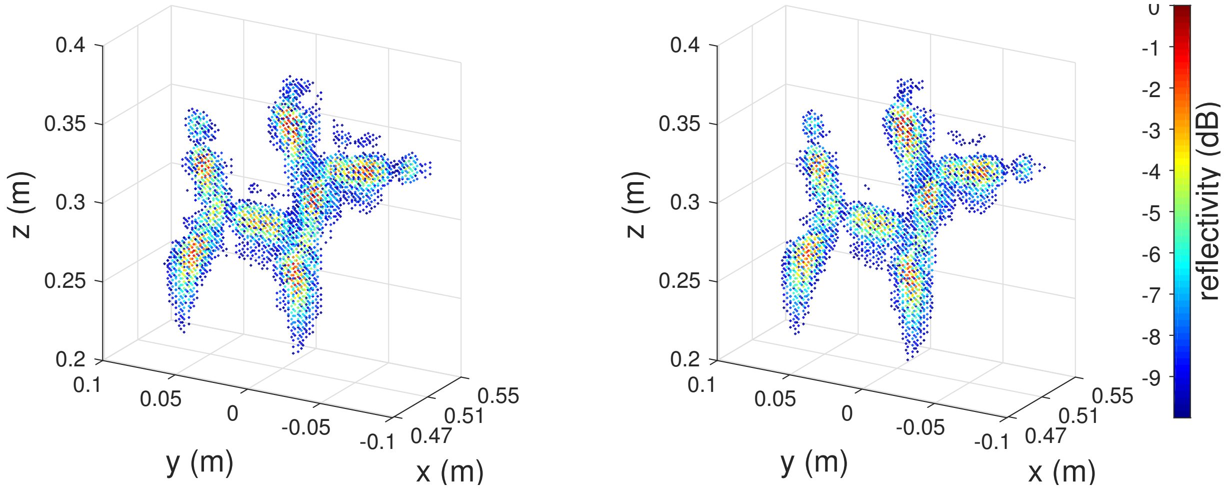

(c) PMF (d) PPI

Figure 5.3: (a) photo of the scene, (b) matched filter reconstruction, (c) partitioned matched filter reconstruction, (d) partitioned pseudo inverse reconstruction.

TABLE 1

Time for 3D image reconstruction.

	MF	PMF	PPI
CPU (single core)	149615 s (1 X - reference time)	1644 s (91 X speedup)	1648 s (91 X speedup)
CPU (4 cores)	95287 s (1.6 X speedup)	1588 s (94 X speedup)	1597 s (94 X speedup)
GPU	12847 s (11.5 X speedup)	41 s (3649 X speedup)	50 s (2992 X speedup)

trix and its inversion. However, as the reconstruction matrix can be computed offline, the reconstruction time reduces to 41 s for both cases. This is a 300 X speedup compared with the conventional unpartitioned matched filter reconstruction run on a GPU. The GPU performance was compared with the performance of a Intel Core i7-6700 CPU at 3.4 GHz with 16 GB memory, using a single core and four-cores. All the timings in Table 1 are compared against the matched filter reconstruction using a single core. For multi-core CPU processing, the algorithms were implemented using MATLABs SPMD (single program, multiple data) functionality. However, there is a communication overhead involved with parallelism and due to the large amount of data a reasonable improvement was not achieved using multiple parallel cores.

Chapter 6

ENHANCED RESOLUTION 3D IMAGE RECONSTRUCTION WITH DMAS

In this chapter 3D SAR imaging results for a commercial DMA are presented. Imaging is done with enhanced resolution stripmap mode (ERSM) [8] SAR, where the beamsteering abilities of the DMA are utilized to increase the virtual antenna beamwidth, and hence achieve a finer cross range resolution. However, this increases the number of measurements collected and the reconstruction is even more computationally complex than the standard stripmap mode SAR. Therefore, PI algorithms are applied to accelerate the image reconstruction.

6.1 3D ERSM for DMA

As discussed in Chapter 2, DMAs have shown to be a promising approach for SAR imaging. The flexibility of DMAs can be used to improve SAR imaging in many ways. In [8] an enhanced resolution stripmap mode (ERSM) for DMAs was introduced to achieve a finer cross-range resolution while maintaining a larger scene coverage (as with standard stripmap mode SAR). As analysed in Chapter 2 [see (2.5)] cross-range resolution is inversely proportional to the beamwidth of the antenna. Hence, a larger antenna beamwidth would improve the cross-range resolution. The idea of ERSM SAR is to create a large virtual antenna beamwidth by steering the antenna. Proof of concept experimental results were presented in [8] for 2D SAR imaging. In this work ERSM is extended to 3D SAR imaging. In 3D ERSM, the antenna is steered to create a large virtual beamwidth at each position of the

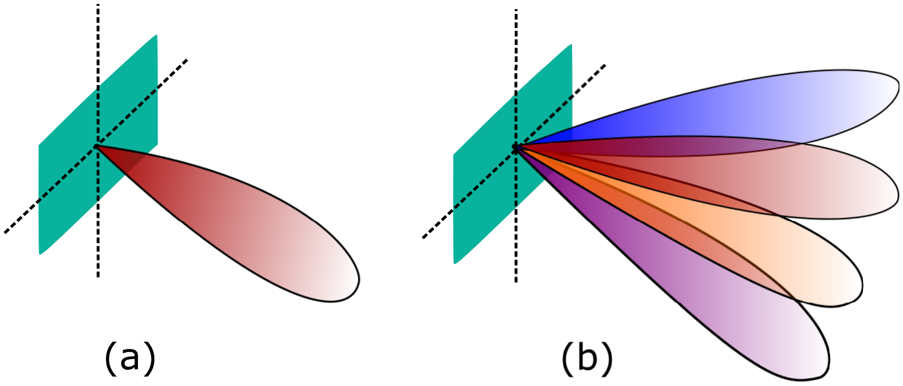

Figure 6.1: Beamsteering of a DMA: (a) beam in broadside ($\alpha = 90°$, $\beta = 0°$), (b) beam steering for ERSM.

scan. Fig. 6.1 illustrates the beamsteering for ERSM with a DMA.

6.2 PI Algorithms for 3D ERSM

In contrast to the standard stripmap mode SAR, where only one measurement is collected at each antenna position, in the 3D ERSM SAR approach, multiple measurements are collected. This accumulates a larger amount of data to be processed and the reconstruction gets more time consuming.

The PI algorithms developed in this thesis can be extended for 3D ERSM SAR imaging to accelerate the reconstruction. In the standard stripmap mode SAR, looking angle α and squint angle β are fixed. Therefore, only one sub-measurement matrix is needed across all the partitions. In 3D ERSM SAR multiple steering angles are used. However the same set of steering angles are used across all the positions. Therefore PI algorithms can be applied to reconstruct the image for individual steering angles separately. The final image can be reconstructed by coherently adding the individual reconstructions. With the availability of high performance hardware, the processing of the individual reconstructions can also be done in parallel.

6.3 Echodyne MESA

For the work discussed in this chapter, a K-band metamaterial electronically scanning array (MESA) developed by Echodyne Corporation (Bellevue, WA, USA) is used (see Fig. 6.2). The MESA has a narrow beam of 4° in azimuth and 12° in elevation, and is able to steer 60° in azimuth and 40° in elevation with 2° steps. The center frequency is in the band of 20 GHz to 24.5 GHz.

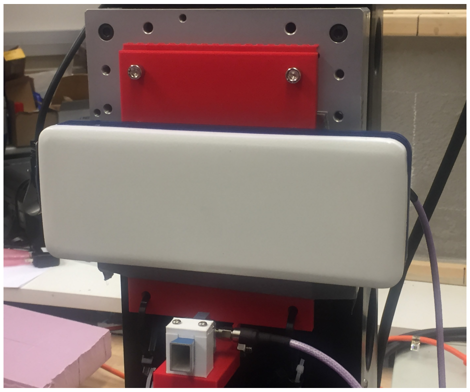

Figure 6.2: Metamaterial Electronically Scanning Array developed by Echodyne Corporation.

6.4 SAR Imaging Results

In this section, experimental results using 3D ERSM SAR imaging are presented. While the transmission is done using the MESA, a K-band horn antenna is used to receive the signal. Frequencies from 15 GHz to 26.5 GHz are used, spaced at 100 MHz intervals. The antenna platform is moved 0.592 m in both the elevation and the azimuth at a spacing of 4 mm. At each position the beam is steered in 13 directions, with looking angles $\alpha = [98°, 98°, 98°, 98°, 90°, 90°, 90°, 90°, 90°, 82°, 82°, 82°, 82°]$ and squint angles $\beta = [6°, 2°, -2°, -6°, 8°, 4°, 0°, -4°, -8°, 6°, 2°, -2°, -6°]$. The projected beam pattern at 1.2 m in ground-range is shown in Fig. 6.3. Note that in the standard stripmap mode (SM) boresight measurements are taken with $\alpha = 90°$ and $\beta = 0°$.

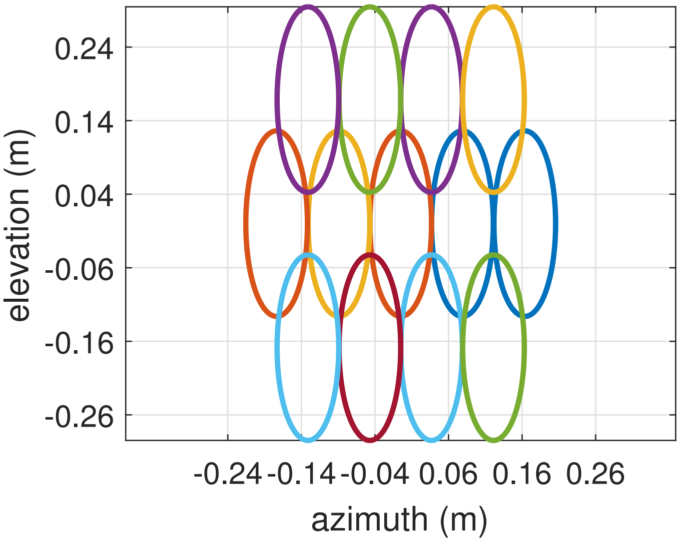

Figure 6.3: Projected beampattern used for 3D ERSM SAR.

Even though the MESA has narrow beamwidths of 4° and 12°, the actual beamwidth seems to be much larger due to sidelobes. For the PI reconstructions, it was empirically found that the effective beamwidths are around 35°. As with the other experimental framework in this thesis, transfer function measurements at each position are collected using an Agilent A5222N vector network analyzer. The reconstruction scene consists of letters U and W and 2 distinct point targets made out of screws in 3D as shown in Fig. 6.4. The scene is 0.5 m in

Figure 6.4: Photo of the scene.

ground-range, 2.0269 m in azimuth and 2.0392 m in elevation. The spacing between voxels is 4 mm. The reconstruction was performed in MATLAB.

6.4.1 Resolution Analysis

In Fig. 6.5 the cross-range resolution is analysed using a measured PSF. MF is used for reconstruction. In the image reconstructed using standard SM SAR the azimuth resolution is 1.9 cm and the elevation resolution is 1.4 cm. In the image reconstructed using ERSM SAR the azimuth resolution is 1.4 cm and the elevation resolution is 1.3 cm. The azimuth resolution has clearly improved with the use of ERSM SAR (26 % improvement).

However, the expected improvement in elevation resolution has not been achieved. The reason could be that the sidelobes in DMA induced a wider elevation beamwidth, and in the standard SM measurements the antenna illuminated the entire scene in elevation. Hence a near optimal resolution is achieved even without ERSM SAR.

The ground-range information has also improved with the 3D ERSM SAR. The azimuth-ground-range plane (x-y plane) of the reconstruction of an isolated screw is shown in Fig. 6.6.

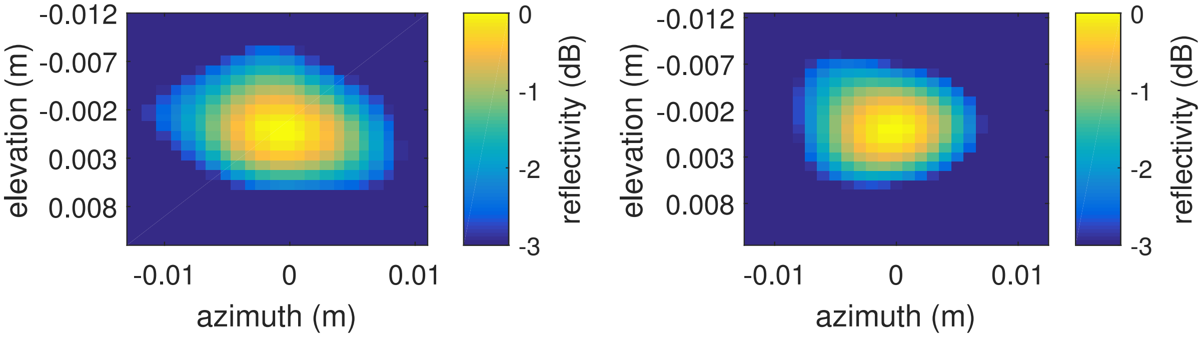

(a) MF standard SM

(b) MF ERSM

Figure 6.5: Measured PSF from DMA reconstructed with MF: (a) Standard SM, (b) ERSM.

The length of the screw is 2.29 cm. When using standard SM measurements, the reconstruction spans 7.5 cm in ground-range while using ERSM measurements it spans only 4.3 cm (42 % improvement). This improvement is due to the fact that in ERSM SAR the antenna is looking at the screw in different angles and hence more information is captured. It should be noted that in the reconstruction, the screw is skewed towards an angle. It is believed that the spiral threading of the wood screw causes this effect.

6.4.2 Accelerated reconstruction

In this section, SAR imaging results with applying PI algorithms to reconstruct 3D ERSM measurements are presented. Both PMF and PPI are used for reconstruction. In PPI 44 singular values are retained when regularizing the sub-measurement matrices. The 3D reconstruction with a GPU acceleration took 41.9 hrs, 1.78 hrs and 1.93 hrs with MF, PMF and PPI respectively. PI algorithms are 23.5 times faster the MF. The cross-range planes of the reconstructed U and W are shown in Fig. 6.7. There is visibly no difference between

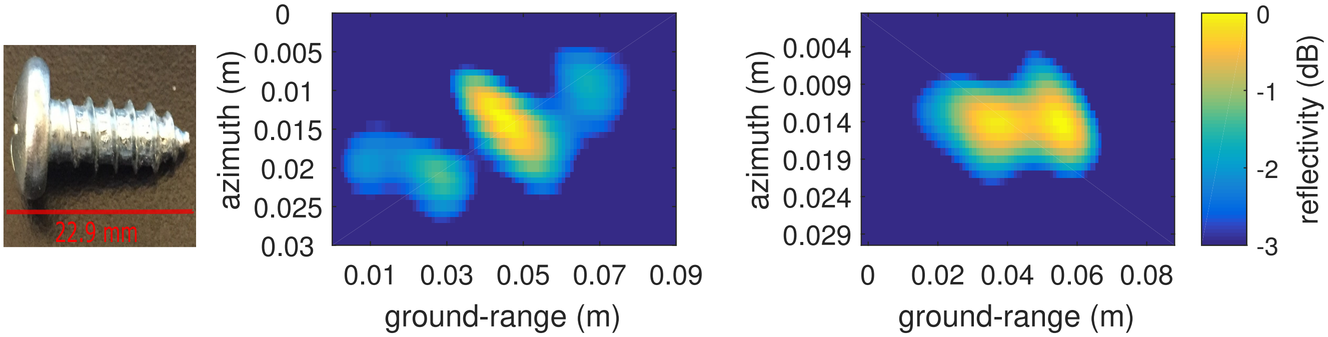

(a) Screw (b) MF standard SM (c) MF ERSM

Figure 6.6: x-y plane of a measured screw reconstructed with MF: (a) photo of the scew, (b) standadrd SM, (c) ERSM.

the reconstructed images using MF, PMF and PPI for 3D ERSM. Note that since letter W is farther away than U, the reflections are weaker.

Based on the results, it can be concluded that PI algorithms along with 3D ERSM can be applied to improve 3D SAR imaging.

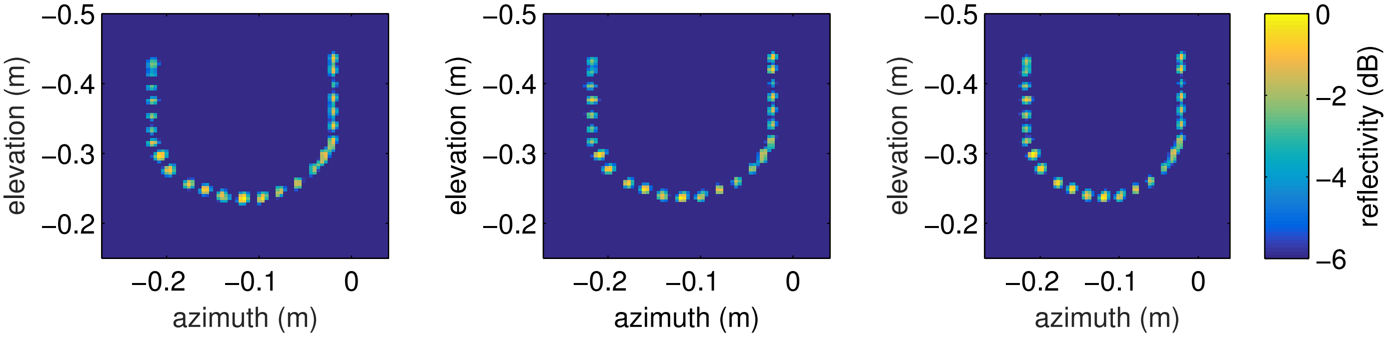

(a) MF (b) PMF (c) PPI

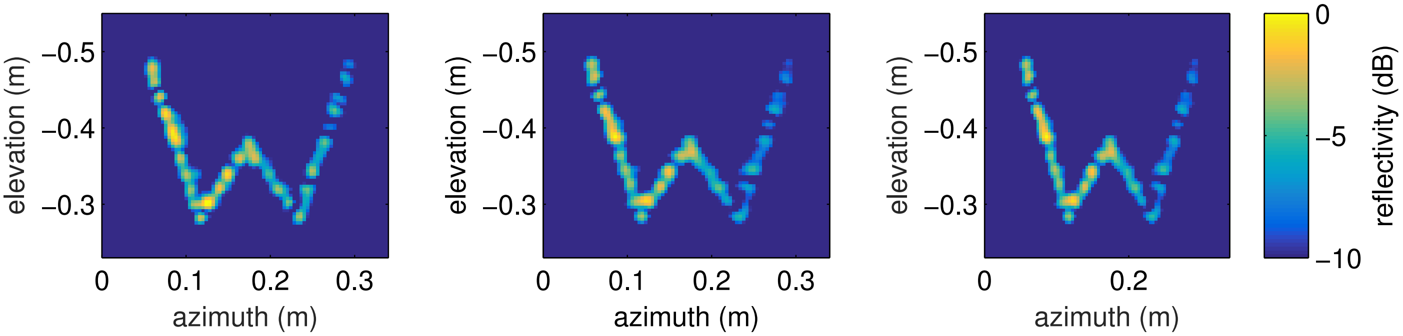

(d) MF (e) PMF (f) PPI

Figure 6.7: y-z plane of the letters U and W reconstruction using ERSM measurements with: (a) & (d) MF, (b) & (e) PMF, (c) & (f) PPI.

Chapter 7

IMAGE RESTORATION USING PSF DECONVOLUTION FOR DMAS

In this chapter, results using a liquid-crystal based dynamic metasurface antenna for near-field SAR imaging are presented. Due to the effect of side lobes in the radiation pattern, the obtained SAR images are distorted and smeared by the point spread function (PSF). This work shows that Lucy-Richardson deconvolution using a measured PSF can be applied to correct the smearing, achieve high resolution, and restore the image. Furthermore, the reconstruction is accelerated for strip map mode imaging using partitioned inverse algorithms.

7.1 Liquid-Crystal-Based DMA

As discussed in Section 2.4, dynamic metasurface antennas (DMA) have many advantages over electronically steered antenna arrays and can be used for SAR imaging. For the work discussed in this chapter, a commercial prototype of a X-band DMA (see Fig. 7.1) developed by Kymeta Corporation (Redmond, WA, USA) using liquid crystal technology is used. This particular DMA was originally designed for communication applications, hence, it has a narrow beam of about 5° and a center frequency of 11.85 GHz. The DMA has over 6,000 sub-wavelength radiating metasurface elements. Each of the elements has an independent electronic control via electric-field excitation of a liquid crystal dielectric layer. The DMA is able to steer the spherical angles up to 70° and is able to change its polarization.

The SAR imaging was done in the near-field of the antenna. Hence, due to the effect of

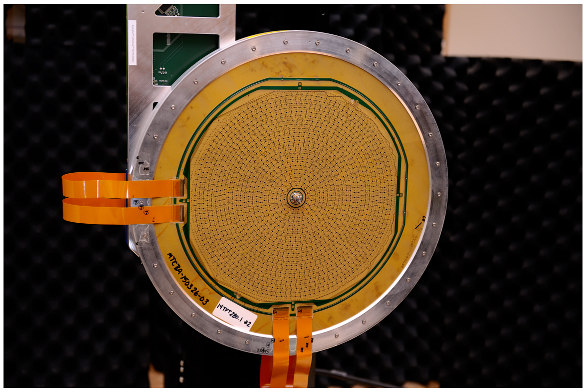

Figure 7.1: Commercial prototype of a DMA, developed by the Kymeta Corporation.

the side lobes, the obtained PSF is not an expected sinc pulse, but rather a distorted version (see Fig. 7.2). As visible in Fig. 7.4 the images obtained are also smeared by the PSF.

7.2 PSF Deconvolution

PSF deconvolution is a widely used operation in image processing to deblur images [32, 33, 34], which has been adapted to radio wave imaging as well. The most commonly used algorithms for deconvolution are blind deconvolution [35], Lucy-Richardson deconvolution [35], regularized deconvolution [36], and Wiener deconvolution [36].

Deconvolution has been used to enhance results of near field microwave imaging. Since it is hard to model the PSF in the near field, blind deconvolution has been proposed as a solution [37, 38]. In [39], the authors present a model of a millimeter wave radar system for suicide bomber detection. Explosive compounds like TNT are weak dielectric scatters, for which the SAR image is highly corrupted by the PSF. The authors proposed to use regularized deconvolution algorithm to remove the blurring effect introduced by PSF.

Deconvolution is applied when the image is smeared by the PSF. That is, the value of each pixel is replaced by a weighted sum of its original value and that of the neighbouring pixels. This can be represented as a form of convolution, hence,

$$\mathbf{Y} = \mathbf{X} * \mathbf{S} \tag{7.1}$$

where $\mathbf{X}$ is the original image, $\mathbf{S}$ is the PSF, $\mathbf{Y}$ is the degraded image, and $*$ denotes the 2D convolution operator.

According to (7.1), $\mathbf{X}$ can be found by applying a 2D deconvolution operation to $\mathbf{Y}$. Since convolution translates to multiplication in frequency domain, this can be implemented quite easily in the frequency domain. This is similar to the inverse filtering discussed in Chapters 3 and 4. It was discussed that in presence of noise, PSF had a significant resolution and a peak was achievable only in the absence of noise. Similarly when noise is present, the noise is not convolved with the PSF and a simple deconvolution operation will not result in restoring the original image [34].

Hence, in this work Lucy-Richardson (LR) deconvolution, which is based on maximum likelihood, is used for image restoration.

LR deconvolution does not directly invert the process of convolution. Instead the process estimates an image which, when blurred by the PSF, is as close as possible to the observed image. This iteration process was separately proposed by William Richardson [40] and Leon Lucy [41]. The LR algorithm was developed based on the Bayess theorem and is explained in the following:

Let X_i denote the i^{th} location in the array $\mathbf{X}$ or the value associated with the i^{th} location and $X = \sum_i X_i$. The idea is to estimate the most likely original X_i, given Y_k and $S_{i,k}$. Here $S_{i,k}$ is the fraction of reflectivity coming from 'i' and observed at 'k'.

Considering all Y_k and their dependencies on X_i,

$$P(X_i) = \sum_k P(X_i|Y_k)P(Y_k). \tag{7.2}$$

From Bayes theorem,

$$P(X_i|Y_k) = \frac{P(Y_k|X_i)P(X_i)}{\sum_i P(Y_k|X_i)P(X_i)}. \tag{7.3}$$

Substituting (7.3) in (7.2) leads to,

$$P(X_i) = P(X_i)\sum_k \frac{P(Y_k|X_i)P(Y_k)}{\sum_i P(Y_k|X_i)P(X_i)}. \tag{7.4}$$

Here, $P(X_i)$ is the desired solution, yet it is also a term on the right hand side. Since $P(X_i)$ is not known, the accepted practice [40] is to iteratively estimate $P(X_i)$ until it converges. Hence, the iteration is defined as

$$P(X_i^{t+1}) = P(X_i^t)\sum_k \frac{P(Y_k|X_i)P(Y_k)}{\sum_i P(Y_k|X_i)P(X_i^t)}. \tag{7.5}$$

Because of (7.1),

$$P(Y_k|X_i) = P(S_{i,k}). \tag{7.6}$$

Furthermore,

$$P(X_i) = \frac{X_i}{X}. \tag{7.7}$$

Assuming $\mathbf{X}, \mathbf{Y}$ and $\mathbf{S}$ are all of same size,

$$X_i^{t+1} = X_i^t \sum_k \frac{S_{i,k}Y_k}{\sum_i S_{i,k}X_i^t}, \tag{7.8}$$

which can be rewritten in terms of the convolution operator [35] as

$$\mathbf{X}^{t+1} = \mathbf{X}^t(\frac{\mathbf{Y}}{\mathbf{X}^t * \mathbf{S}} * \mathbf{S}'). \tag{7.9}$$

where $\mathbf{S}'$ is the spatial reversed PSF.

7.3 SAR Imaging Results

In this section, experimental 2D imaging results using the aforementioned approach are presented. While the transmission is done using the liquid-crystal based DMA, an X-band horn antenna is used to receive the signal. The antenna platform is moved 0.592 m in the azimuth direction at a spacing of 8 mm and a looking angle of 70°. The height of the platform is 0.2737 m. Frequencies from 10 GHz to 13.7 GHz are used, spaced at 10 MHz intervals. Even though the DMA has a narrow beamwidth of 5°, sidelobes induced aliasing was visible with PI reconstructions. Hence, 60° is considered as the effective beamwidth for PI algorithms. At each antenna position, transfer function measurements are collected using an Agilent A5222N vector network analyzer. The reconstruction scenes are 0.5 m in ground-range and 1.5 m in azimuth. The azimuth dimension was chosen to reconstruct the scene as observed by all antenna positions. The spacing between voxels is 1 mm. In the images, the reflectivity is normalized presented on a logarithmic scale. The reconstruction was performed in MATLAB.

7.3.1 Point Spread Function

In this section the measured PSF is analyzed. Fig. 7.2 depicts the PSF reconstructed from MF, PMF, and PPI for the strip-map mode. Optimal number of singular values to be kept for PPI reconstruction was found as 11 with the use of L-curves. The reconstruction took 290 s with MF, 13 s with PMF and 38.5 s with PPI with GPU acceleration. When applying LR deconvolution, the resolution of the PSF changes with the number of iterations carried out. If the proper number of iterations are carried out, a peak can be obtained for the PSF. Fig. 7.3 illustrates how the resolution of the PSF changed with the number of iterations for different reconstruction algorithms. It can be seen from the Fig. 7.3b, that in the azimuth

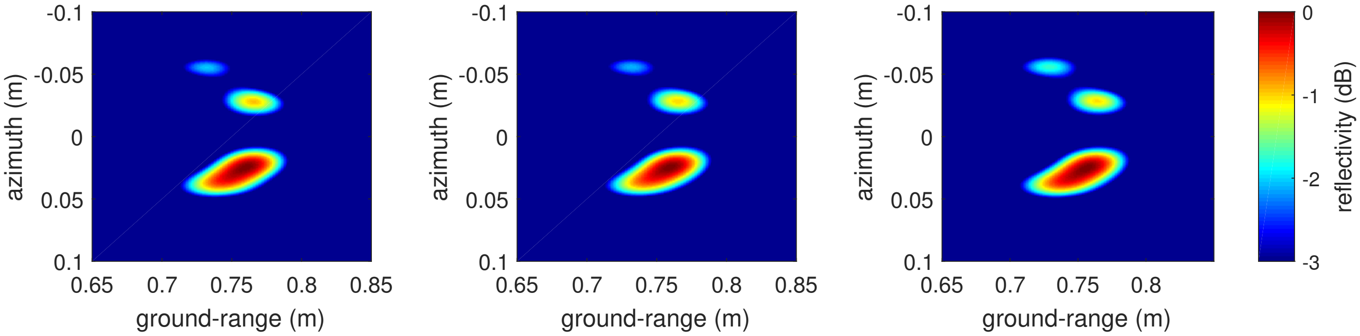

(a) MF

(b) PMF

(c) PPI

Figure 7.2: Measured PSF from DMA: (a) MF reconstruction, (b) PMF reconstruction, (c) PPI reconstruction (11 singular values retained).

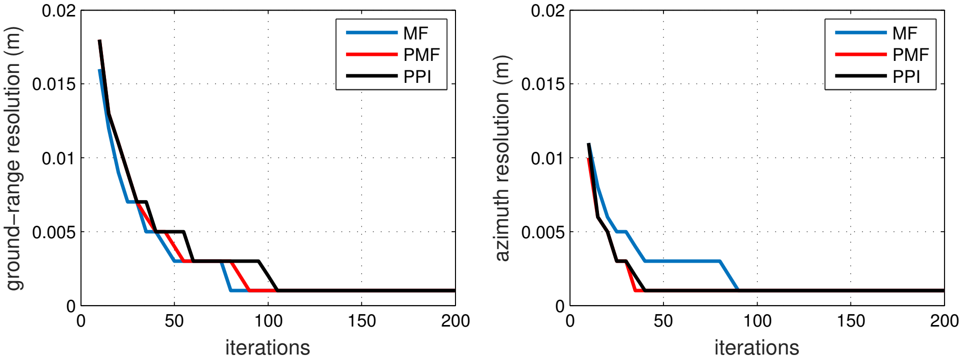

(a)

(b)

Figure 7.3: Resolution after LR deconvolution against number of iterations: (a) ground-range resolution, (b) azimuth resolution.

direction the PSF converges to a peak quickly when using the PI algorithms.

7.3.2 2D images

In Fig. 7.4a and 7.4b the scenes to be imaged, letters U and W are shown. The reconstructions were done using MF, PMF, and PPI. The optimal singular values to be retained with PPI reconstruction was found as 15 for both the scenes. The average reconstruction times per scene were 289 s, 14 s, 43 s for MF, PMF, and PPI respectively (with GPU acceleration). The speedup with PMF over MF is 20.6X and the speedup with PPI over MF is 6.7X. For the experiments a finer frequency spacing was chosen (10 MHz in contrast to 100 MHz) to achieve better quality images and hence the speedup with PPI is relatively low in this experiment as compared to the other experiments in this thesis. However, as the construction and the inversion of the sub-measurement can be done offline, the timings for PPI can be improved to be as effective as PMF. The images before deconvolution and after deconvolution are compared and the effect of LR deconvolution is quite visible. (LR deconvolution was done using 80 iterations). Before applying deconvolution the letters U and W are not distinguishable. After the deconvolution operation, the letters are clearly distinguishable as the resolution of the point sources has improved. However, not all the points are visible after restoration due to the interference from the nearby points.

7.3.3 Spot Light Mode Imaging

The advantage of using DMAs is their beam steering capabilities, which the strip-map mode does not utilize. Spot-light mode on the other hand utilize beam steering as the antenna is always illuminating a certain area. In this section, SAR imaging results of spot-light mode using liquid-crystal-based DMA is presented. The reconstruction scene consists of 11 point sources, separated by 4 cm in azimuth direction.

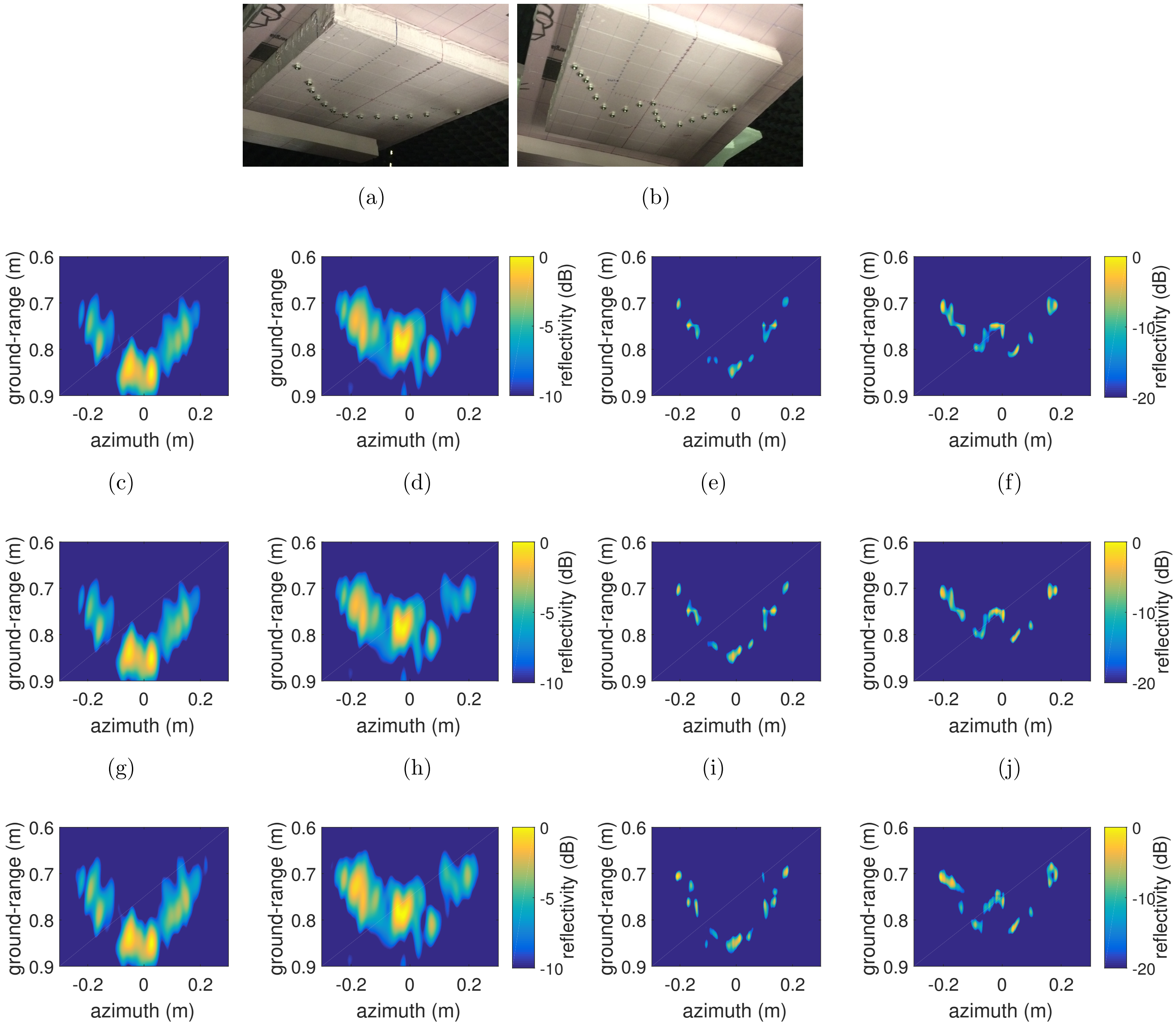

(a) (b)

(c) (d) (e) (f)

(g) (h) (i) (j)

(k) (l) (m) (n)

Figure 7.4: Experimental results: (a)-(b) Photos of letters U and W, (c)-(d) MF reconstruction, (e)-(f) MF reconstruction with LR deconvolution, (g)-(h) PMF reconstruction, (i)-(j) PMF reconstruction with LR deconvolution, (k)-(l) PPI reconstruction, (m)-(n) PPI reconstruction with LR deconvolution.

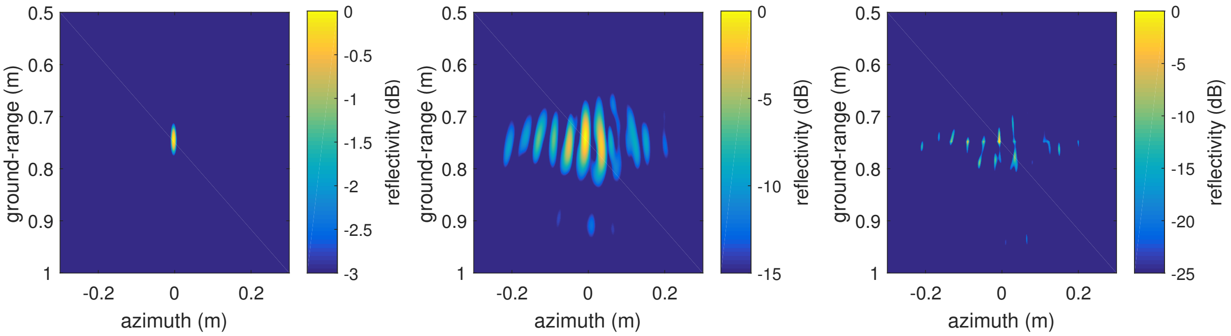

(a) (b) (c)

Figure 7.5: Spot light mode imaging with DMA: (a) Measured PSF, (b) MF reconstruction, (c) MF reconstruction with LR deconvolution.

The reconstruction was done only using MF, as the PI algorithms are not optimized for spot-light mode imaging. Fig. 7.5a shows the measured PSF for spot-light mode. Fig. 7.5b is the reconstructed scene and Fig. 7.5c is the result of LR deconvolution (with 80 iterations). Once again, the resolution of the point sources has improved after applying the deconvolution. The diffraction patterns of the point sources are also visible as the reflectivity intensity is not thresholded.

In this work, the deconvolution was carried out using only the magnitude information of the reflectivity values. The deconvolution using complex values is subject to future research.

Chapter 8

CONCLUSION

In this thesis, computational imaging was used to improve millimeter-wave dynamic metasurface based synthetic aperture radar (SAR) image reconstruction.

SAR image reconstruction is a computationally complex inverse problem, which can be solved via a generalized inverse, e.g. full pseudo inverse (FPI), or be approximated, e.g. matched filter (MF). In the first part of the thesis, a computationally efficient partitioned inverse (PI) algorithm was proposed for SAR image reconstruction. The independent partitions were reconstructed in parallel using the matched filter or the pseudo inverse. A parallelized approach leveraging a graphics processing unit (GPU) was used to achieve a dramatic speedup compared to non-GPU accelerated algorithms. In the results presented in this thesis, PI algorithms were three orders magnitude faster than the FPI and two orders faster than the MF. The improved resolution of FPI was maintained by using the pseudo inverse to find the solutions for the PI. The partitioned pseudo inverse (PPI) algorithm is based on the Moore-Penrose pseudo inverse, using truncated singular value decomposition for regularization. Optimal regularization ensures that the algorithm is robust to noise. It was shown that the PPI has an improved resolution of 24% over MF even at 0 dB SNR. Experimental results using a laboratory K-band (15-26.5 GHz) ultra-wideband SAR system were presented to validate the PI algorithms. Even though PMF was faster than PPI, as the computation of sub-measurement matrix and its inversion can be done off-line, PPI was just as efficient. This work is published in [5, 6].

The second part of the thesis focused on SAR imaging with dynamic metasurface antennas (DMA). Enhanced resolution stripmap mode (ERSM) SAR approach was extended for 3D imaging using DMA, where PI algorithms were used to accelerate the reconstruction. Experimental results using a commercial prototype DMA were presented. It was shown that the cross-range resolution and ground-range resolution improved by 26% and 42%, respectively when using 3D ERSM SAR. Furthermore, the PI reconstruction resulted in a 23.5X speedup over the MF. A limitation with the use of DMAs for SAR imaging are the strong antenna side lobes, which caused the reconstructed images to be smeared by the distorted point spread function (PSF). It was shown that Lucy-Richardson deconvolution using a measured PSF can correct the smearing, achieve high resolution and restore the image. Experimental results using a liquid-crystal based DMA for near field SAR imaging were presented, where the reconstructed images were restored using Lucy-Richardson deconvolution.

PI algorithms has promise as an alternative inverse filtering method for SAR which avoids the time and memory constrains of the full inverse, while maintaining the improved resolution. They can be combined with stochastic sampling to reduce the number of measurements and make the imaging process more efficient.

BIBLIOGRAPHY

[1] R. Appleby and R. N. Anderton, "Millimeter-wave and submillimeter-wave imaging for security and surveillance," *Proceedings of the IEEE*, vol. 95, pp. 1683–1690, Aug 2007.

[2] D. M. Sheen, D. L. McMakin, and T. E. Hall, "Three-dimensional millimeter-wave imaging for concealed weapon detection," *IEEE Transactions on Microwave Theory and Techniques*, vol. 49, pp. 1581–1592, Sep 2001.

[3] J. Hunt, J. Gollub, T. Driscoll, G. Lipworth, A. Mrozack, M. S. Reynolds, D. J. Brady, and D. R. Smith, "Metamaterial microwave holographic imaging system," *Journal of the Optical Society of America A*, vol. 31, pp. 2109–2119, Oct 2014.

[4] R. Solimene, I. Catapano, G. Gennarelli, A. Cuccaro, A. Dell'Aversano, and F. Soldovieri, "SAR imaging algorithms and some unconventional applications: A unified mathematical overview," *IEEE Signal Processing Magazine*, vol. 31, pp. 90–98, July 2014.

[5] S. Devadithya, A. Pedross-Engel, C. M. Watts, and M. S. Reynolds, "Partitioned inverse image reconstruction for milimeter-wave SAR imaging," in *IEEE International Conference on Acoustics, Speech and Signal Processing (ICASSP)*, IEEE, March 2017.

[6] S. Devadithya, A. Pedross-Engel, C. M. Watts, and M. S. Reynolds, "GPU accelerated partitioned reconstruction algorithm for millimeter-wave 3D synthetic aperture radar (SAR) images," in *International Microwave Symposium (IMS)*, IEEE, June 2017.

[7] G.-C. Sun, M. Xing, X.-G. Xia, Y. Wu, and Z. Bao, "Beam steering SAR data processing by a generalized PFA," *IEEE Transactions on Geoscience and Remote Sensing*, vol. 51, no. 8, pp. 4366–4377, 2013.

[8] A. Pedross-Engel, C. M. Watts, D. R. Smith, and M. S. Reynolds, "Enhanced resolution stripmap mode using dynamic metasurface antennas," *IEEE Transactions on Geoscience and Remote Sensing*, 2017.

[9] M. Boyarsky, T. Sleasman, L. Pulido-Mancera, T. Fromenteze, A. Pedross-Engel, C. M. Watts, M. F. Imani, M. S. Reynolds, and D. R. Smith, "Synthetic aperture radar with dynamic metasurface antennas: a conceptual development," *Journal of the Optical Society of America A*, vol. 34, no. 5, pp. A22–A36, 2017.

[10] C. M. Watts, A. Pedross-Engel, D. R. Smith, and M. S. Reynolds, "X-band SAR imaging with a liquid-crystal based dynamic metasurface antenna," *Journal of the Optical Society of America B*, vol. 34, pp. 300–306, January 2017.

[11] J. Hunt, T. Driscoll, A. Mrozack, G. Lipworth, M. Reynolds, D. Brady, and D. R. Smith, "Metamaterial apertures for computational imaging," *Science*, vol. 339, no. 6117, pp. 310–313, 2013.

[12] A. Moreira, P. Prats-Iraola, M. Younis, G. K. I. Hajnsek, and K. P. Papathanassiou, "A tutorial on synthetic aperture radar," *IEEE Geoscience and Remote Sensing Magazine*, vol. 1, pp. 6–43, March 2013.

[13] D. C. Munson and R. L. Visentin, "A signal processing view of strip-mapping synthetic aperture radar," *IEEE Transactions on Acoustics, Speech, and Signal Processing*, vol. 37, pp. 2131 – 2147, December 1989.

[14] I. G. Cumming and F. H. Wong, *Digital Processing of Synthetic Aperture Radar Data: Algorithms and Implementation.* Artech House, 2005.

[15] D. Vu, M. Xue, X. Tan, and J. Li, "A Bayesian approach to SAR imaging," *Digital Signal Processing*, vol. 23, no. 3, pp. 852–858, 2013.

[16] J. Xu, Y. Pi, and Z. Cao, "Bayesian compressive sensing in synthetic aperture radar imaging," *IET Radar, Sonar & Navigation*, vol. 6, no. 1, pp. 2–8, 2012.

[17] S. Samadi, M. Çetin, and M. A. Masnadi-Shirazi, "Sparse representation-based synthetic aperture radar imaging," *IET radar, sonar & navigation*, vol. 5, no. 2, pp. 182–193, 2011.

[18] A. Achim, P. Tsakalides, and A. Bezerianos, "SAR image denoising via bayesian wavelet shrinkage based on heavy-tailed modeling," *IEEE Transactions on Geoscience and Remote Sensing*, vol. 41, no. 8, pp. 1773–1784, 2003.

[19] M. Albuquerque, P. Prats, and R. Scheiber, “Applications of time-domain back-projection SAR processing in the airborne case,” in *Synthetic Aperture Radar (EUSAR), 2008 7th European Conference on*, pp. 1–4, VDE, 2008.

[20] J. W. McCorkle and M. Rofheart, “Order Nˆ2log(N) backprojector algorithm for focusing wide-angle wide-bandwidth arbitrary-motion synthetic aperture radar,” in *Aerospace/Defense Sensing and Controls*, pp. 25–36, International Society for Optics and Photonics, 1996.

[21] Y. Ding and D. J. Munson, “A fast back-projection algorithm for bistatic SAR imaging,” in *Image Processing. 2002. Proceedings. 2002 International Conference on*, vol. 2, pp. II–II, IEEE, 2002.

[22] S. Xiao, D. C. Munson, S. Basu, and Y. Bresler, “An Nˆ2log(N) back-projection algorithm for SAR image formation,” in *Signals, Systems and Computers, 2000. Conference Record of the Thirty-Fourth Asilomar Conference on*, vol. 1, pp. 3–7, IEEE, 2000.

[23] P. A. Rosen, S. Hensley, S. Shaffer, L. Veilleux, M. Chakraborty, T. Misra, R. Bhan, V. R. Sagi, and R. Satish, “The NASA-ISRO SAR mission-an international space partnership for science and societal benefit,” in *Radar Conference (RadarCon), 2015 IEEE*, pp. 1610–1613, IEEE, 2015.

[24] R. J. Mailloux, *Phased array antenna handbook*, vol. 2. Artech House Boston, 2005.

[25] T. Sleasman, M. Boyarsky, L. Pulido-Mancera, T. Fromenteze, M. F. Imani, M. Reynolds, and D. R. Smith, “Experimental synthetic aperture radar with dynamic metasurfaces,” *arXiv preprint arXiv:1703.00072*, 2017.

[26] W. Meneke, *Geophysical Data Analysis:Discrete Inverse Theory.* Academic Press, London: International Geophysics Series, 1984.

[27] O. Yurduseven, J. Gollub, H. Odabasi, M. F. Imani, G. Lipworth, A. Rose, P. Trofetter, and D. R. Smith, “Comparison of different reconstruction algorithms for image reconstruction in metamaterial aperture based imaging system,” *European Conference on Antennas and Propagation*, January 2015.

[28] C. R. Vogel, *Computational Methods for Inverse Problems.* Philadelphia: Society for Industrial and Applied Mathematics, 2002.

[29] A. Tikhonov, "Solution of incorrectly formulated problems and the regularization method," in *Soviet Math. Dokl*, vol. 4, pp. 1035–1038, 1963.

[30] M. Cetin, I. Stojanovic, O. Onhon, K. Varshney, S. Samadi, W. C. Karl, and A. S. Willsky, "Sparsity-driven synthetic aperture radar imaging: Reconstruction, autofocusing, moving targets, and compressed sensing," *IEEE Signal Processing Magazine*, vol. 31, no. 4, pp. 27–40, 2014.

[31] P. C. Hansen and D. P. O'Leary, "The use of the L-curve in the regularization of discrete ill-posed problems," *SIAM Journal on Scientific Computing*, vol. 14, no. 6, pp. 1487–1503, 1993.

[32] P. C. Hansen, J. G. Nagy, and D. P. O'leary, *Deblurring images: matrices, spectra, and filtering.* SIAM, 2006.

[33] T. S. Ralston, D. L. Marks, F. Kamalabadi, and S. A. Boppart, "Deconvolution methods for mitigation of transverse blurring in optical coherence tomography," *IEEE Transactions on Image Processing*, vol. 14, no. 9, pp. 1254–1264, 2005.

[34] Y. Liu, Y. Liang, G. Mu, and X. Zhu, "Deconvolution methods for image deblurring in optical coherence tomography," *Journal of the Optical Society of America A*, vol. 26, no. 1, pp. 72–77, 2009.

[35] D. Fish, J. Walker, A. Brinicombe, and E. Pike, "Blind deconvolution by means of the Richardson-Lucy algorithm," *Journal of the Optical Society of America A*, vol. 12, no. 1, pp. 58–65, 1995.

[36] R. C. Gonzalez and R. E. Woods, *Digital Image Processing.* Addison-Wesley Publishing Company, Inc., 1992.

[37] A. Mohammad-Djafari, N. Qaddoumi, and R. Zoughi, "Blind deconvolution approach for resolution enhancement of near-field microwave images," in *SPIE's International Symposium on Optical Science, Engineering, and Instrumentation*, pp. 274–281, International Society for Optics and Photonics, 1999.

[38] R. K. Amineh, M. Ravan, A. Trehan, and N. K. Nikolova, "Near-field microwave imaging based on aperture raster scanning with TEM horn antennas," *IEEE Transactions on Antennas and Propagation*, vol. 59, no. 3, pp. 928–940, 2011.

[39] J. A. Martinez-Lorenzo, F. Quivira, and C. M. Rappaport, “SAR imaging of suicide bombers wearing concealed explosive threats,” *Progress In Electromagnetics Research*, vol. 125, pp. 255–272, 2012.

[40] W. H. Richardson, “Bayesian-based iterative method of image restoration,” *Journal of the Optical Society of America*, vol. 62, no. 1, pp. 55–59, 1972.

[41] L. B. Lucy, “An iterative technique for the rectification of observed distributions,” *The astronomical journal*, vol. 79, p. 745, 1974.